

Moiré Band Engineering in Twisted Trilayer WSe₂

Naoto Nakatsuji,¹ Takuto Kawakami,¹ Hayato Tateishi,² Koichiro Kato,² and Mikito Koshino¹

¹*Department of Physics, Osaka University, Toyonaka, Osaka 560-0043, Japan*

²*Department of Applied Chemistry, Kyushu University, Motoooka, Fukuoka 819-0395, Japan*

(Dated: April 30, 2025)

We present a systematic theoretical study on the structural and electronic properties of twisted trilayer transition metal dichalcogenide (TMD) WSe₂, where two independent moiré patterns form between adjacent layers. Using a continuum approach, we investigate the optimized lattice structure and the resulting energy band structure, revealing fundamentally different electronic behaviors between helical and alternating twist configurations. In helical trilayers, lattice relaxation induces $\alpha\beta$ and $\beta\alpha$ domains, where the two moiré patterns shift to minimize overlap, while in alternating trilayers, $\alpha\alpha'$ domains emerge with aligned moiré patterns. A key feature of trilayer TMDs is the summation of moiré potentials from the top and bottom layers onto the middle layer, effectively doubling the potential depth. In helical trilayers, this mechanism generates a Kagome lattice potential in the $\alpha\beta$ domains, giving rise to flat bands characteristic of Kagome physics. In alternating trilayers, the enhanced potential confinement forms deep triangular quantum wells, distinct from those found in bilayer systems. Beyond these bulk states arising from the commensurate domains, the global moiré-of-moiré electronic spectrum exhibits isolated boundary modes localized at domain intersections. Furthermore, we demonstrate that a moderate perpendicular electric field can switch the layer polarization near the valence band edge, providing an additional degree of tunability. In particular, it enables tuning of the hybridization between orbitals on different layers, allowing for the engineering of diverse and controllable electronic band structures. Our findings highlight the unique role of moiré potential summation in trilayer systems, offering a broader platform for designing moiré-based electronic and excitonic phenomena beyond those achievable in bilayer TMDs.

I. INTRODUCTION

Moiré twisted materials have garnered significant attention as platforms for novel quantum phenomena. Twisted bilayer graphene (tBG) serves as a fundamental example, where the moiré-scale modulation of interlayer coupling hybridizes the Dirac cones of monolayer graphene, leading to the formation of flat bands [1–3]. These flat bands drive various correlated states [4–22], including superconductivity, correlated insulator phases, and the anomalous Hall effect.

Beyond graphene-based systems, extensive studies have focused on semiconductor moiré systems, particularly transition metal dichalcogenides (TMDs) [23–103]. In contrast to tBG, moiré TMD bilayers exhibit a dominant moiré intralayer potential, which effectively transforms the system into a triangular array of weakly coupled quantum dots. This provides an ideal platform for investigating Hubbard model physics [23–41], superconductivity [33–46], and unique optical properties such as exciton confinement [47–55]. Additionally, the interplay of moiré intralayer potential and interlayer hopping, as seen in MoTe₂, can generate an effective magnetic field from the non-trivial topological nature, leading to the anomalous Chern insulator [24, 56–69] and fractional Chern insulator phases [61–65, 69–87].

Recent research has expanded to moiré trilayer materials, with twisted trilayer graphene (tTG) being extensively studied as a prototypical system [104–133]. In general trilayer systems, the moiré patterns formed between layers 1 and 2 (moiré 12) and layers 2 and 3 (moiré 23) interfere to create a higher-order moiré-of-moiré pat-

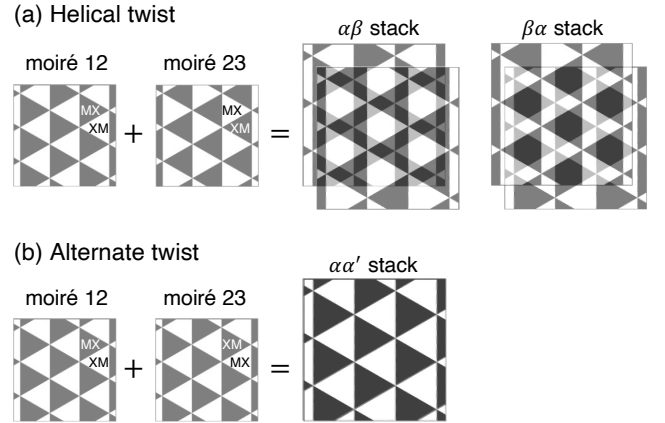


FIG. 1. Schematic figure of the real-space distribution of the potential on the middle layer of twisted trilayer TMD with (a) helical and (b) alternate twist. On each row, the left two panels show the contributions from the moiré pattern between layers 1 and 2 (moiré 12) and between layers 2 and 3 (moiré 23), where darker regions indicate higher potential energy. The right panel displays the total potential in the commensurate domain, obtained by summing the moiré 12 and 23 potentials with the corresponding lateral shift.

tern with a typical length scale of tens to hundreds of nanometers [122–125, 134, 135]. In tTG, structural relaxation induces commensurate domains where the two moiré periodicities locally match, hosting nontrivial topological boundary modes [122, 132–139].

Extending these concepts to trilayer TMDs, previous

studies have investigated commensurate trilayers where the two moiré periods align [140–143]. Here, we examine twisted trilayers of WSe₂ with general twist angles, where two moiré patterns may have different periodicities. We obtain the optimized lattice structure under relaxation and calculate the electronic band structure near the valence band maximum. The system is characterized by twist angles θ_{12} and θ_{23} , and we focus on nearly parallel trilayers with $|\theta_{12}|, |\theta_{23}| \sim 1^\circ$. The physical properties vary strikingly between the helical stack ($\theta_{12}\theta_{23} > 0$) and the alternating stack ($\theta_{12}\theta_{23} < 0$).

The lattice relaxation exhibits trends similar to tTG: in helical trilayers, $\alpha\beta$ and $\beta\alpha$ domains emerge where the moiré lattices shift to minimize overlap, whereas in alternating trilayers, $\alpha\alpha'$ domains form where the two moiré lattices align [See, Fig. 2]. However, the electronic structures differ significantly from tTG. Due to lattice relaxation, moiré interlayer hopping is suppressed, making the band structure primarily determined by the intralayer moiré potentials. The middle layer (layer 2) experiences the combined potential of layers 1 and 3, resulting in a potential twice as large as that of the outer layers. Consequently, the states near the valence band edge are strongly localized in the middle layer.

The spatial configuration of the middle-layer potential exhibits greater diversity than in bilayers. Figure 1 represents the schematic figure of the real-space distribution of the middle-layer potential for (a) helical and (b) alternate twist, where dark region indicates a high potential region. In the helical case, the summation of two triangular potentials from layers 1 and 3 with a spatial translation naturally generates a Kagome lattice potential in $\alpha\beta$, leading to flat bands characteristic of Kagome lattices. In alternating stack, the potentials from layers 1 and 3 coincide in $\alpha\alpha'$ domains, forming triangular quantum wells twice as deep as those in twisted bilayers. In the full moiré-of-moiré band structure, the spectrum consists of cluster of bulk states from $\alpha\beta$, $\beta\alpha$, and $\alpha\alpha'$ domains, along with isolated boundary modes localized at domain corners.

In addition to the intrinsic structural degrees of freedom, twisted trilayer TMDs offer rich opportunities for band structure engineering through external electric fields. By applying a perpendicular electric field, the relative potential of each layer can be selectively tuned, allowing control over the layer polarization of electronic states and the interlayer hybridization between orbitals. This enables the realization of diverse band structures, including graphene-like Dirac bands, flat bands, quadratic band touchings, and hybridized bands formed from various types of orbitals residing on different triangular lattices. Such electrically tunable systems provide a versatile platform to explore correlated electronic phases and topological phenomena in moiré materials.

The paper is organized as follows. In Sec. II, we define the lattice geometry of twisted trilayer TMD and introduce the continuum method used to calculate the optimized lattice structure and electronic properties. We

calculate the optimized lattice structure and its electronic band structure for helical twist in Sec. III, and show the kagome flat band and higher topological flat bands appear on the local $\alpha\beta$ and $\beta\alpha$ stack. In Sec. IV we study alternate twist case, and found the quantum dot states captured the trigonal shape potential. The dependence of the perpendicular electric field is discussed in Sec. V, and we found the various band structures formed from the s -, p - and d -like orbitals of triangular wells. A brief conclusion is provided in Sec. VI.

II. MODEL

A. Geometry of twisted trilayer TMD

Figure 2 illustrates the geometry of a non-relaxed twisted trilayer TMD of helical (upper panels) and alternate stackings (lower panels). Here, θ^{12} denotes the twist angles from layer 1 to 2, and θ^{23} is from layer 2 to 3. The helical and alternate twists correspond to structures with $\theta^{12}\theta^{23} > 0$ and $\theta^{12}\theta^{23} < 0$, respectively. In Figs. 2(b) and (f), we show a schematic figure to illustrate an interference of the two moiré patterns for these structures, where blue and red dots represent the MM stacking point of the moiré 12 (the interference pattern from layer 1 and 2) and the moiré 23 (layer 2 and 3). We define the symbol M, X and O as the transition-metal atom site, and the chalcogen atom site and the vacant site (the center of hexagon), respectively, in a unit cell of monolayer TMD. The MM stacking stands for the arrangement of neighboring layers with M sites vertically aligned.

The interference of the two moiré patterns give rise to a moiré-of-moiré superstructure with a period indicated by a gray region. The local structure approximates a stack of two commensurate moiré lattices with a specific lateral shift. For the helical case, we define three local arrangements $\alpha\alpha$, $\alpha\beta$ and $\beta\alpha$, as shown in Fig. 2(c). Here the filled and open triangles represent the XM and MX domain, respectively, in the individual moiré patterns. In $\alpha\alpha$ structure, the MM stacking points of moiré 12 and those of 23 are aligned, while the $\alpha\beta$ and $\beta\alpha$ stacking take structures with MM stacking points repelled from each other. Figure 2(d) shows the local atomic configurations in $\alpha\alpha/\alpha\beta/\beta\alpha$ structures. For instance, MXO represents a stacking where the M site of layer 1, the X site of layer 2, and the O site of layer 3 are vertically aligned. Note that, unlike trilayer graphene, the $\alpha\beta$ and $\beta\alpha$ structures are not related by a C_{2z} operation, as a monolayer TMDs lacks the C_{2z} symmetry. For the alternate twist, the system hosts three local moiré structure; $\alpha\alpha'$, $\alpha\beta'$ and $\beta\alpha'$ as shown in Figs. 2(g) and 2(h).

In the following, we present a precise description of the geometric configuration for trilayer TMD systems. For TMD, we consider WSe₂ throughout the paper. The primitive lattice vectors a monolayer are given by $\mathbf{a}_1 = a(1, 0)$ and $\mathbf{a}_2 = a(1/2, \sqrt{3}/2)$, where $a \approx 0.33$ nm

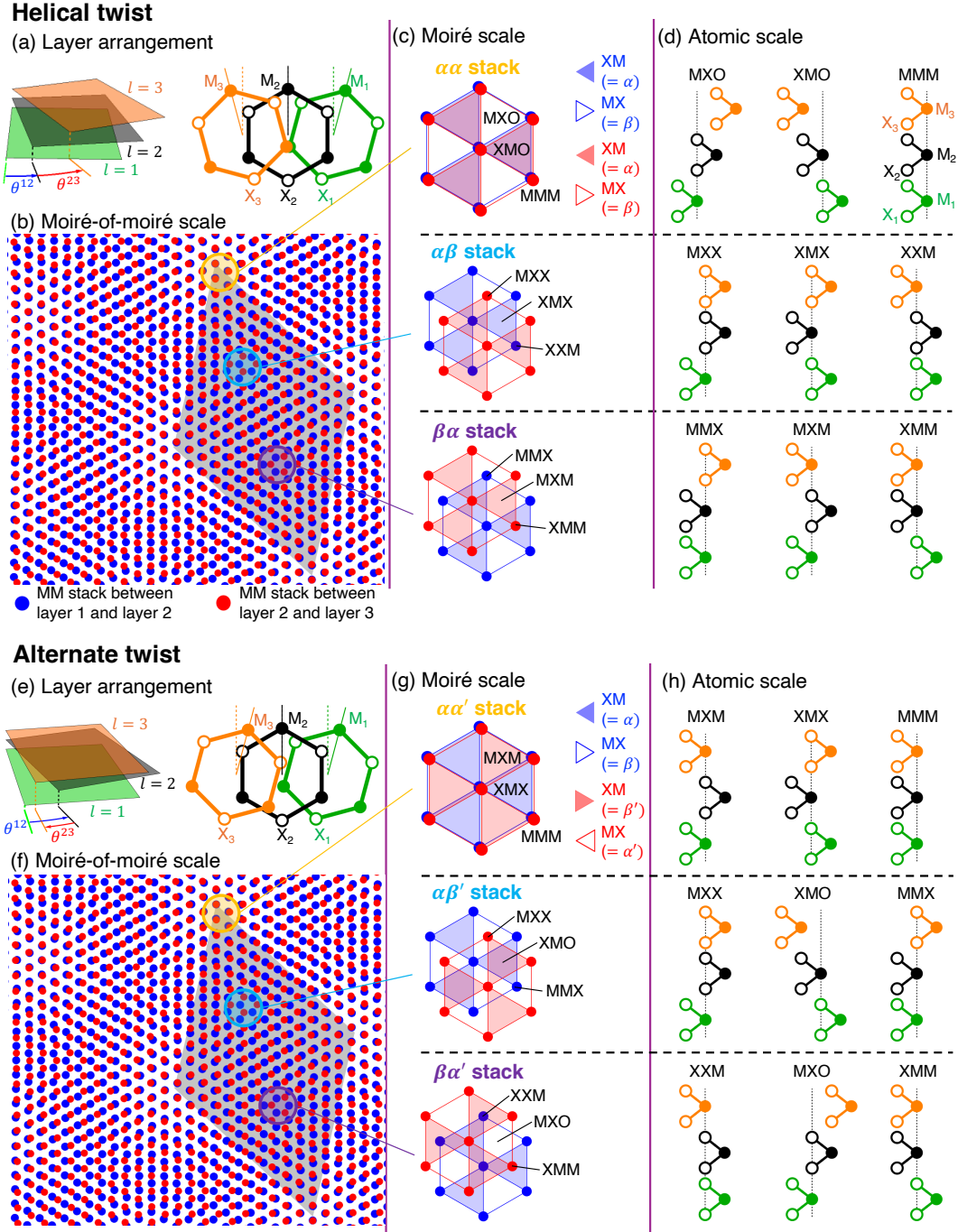


FIG. 2. (a) Stacking geometry of a twisted homo-trilayer TMD with a helical twist. Green, black, and orange sheets represent layers 1, 2, and 3, respectively. (b) Moiré pattern arrangement in the helical twist trilayer. Blue and red dots indicate the MM points of moiré 12 (formed between layers 1 and 2) and moiré 23 (formed between layers 2 and 3), respectively. The gray rhombus marks a moiré-of-moiré unit cell. (c) Representative local moiré structures in (b), where empty and filled triangles denote MX and XM domains, respectively. (d) Side view of the local atomic configurations at specific points in (c). (e-h) Corresponding structures and atomic configurations for the alternate twist case.

is a lattice constant [144]. The lattice vectors of layer $\ell (= 1, 2, 3)$ in the twisted trilayer are written as $\mathbf{a}_j^{(\ell)} = R(\theta^{(\ell)})\mathbf{a}_j$ ($j = 1, 2$), where $R(\theta)$ is a two-dimensional rotation matrix, and $\theta^{(\ell)}$ is the absolute twist angle of layer l specified by $\theta^{(1)} = -\theta^{12}$, $\theta^{(2)} = 0$ and $\theta^{(3)} = \theta^{23}$. Accordingly, the reciprocal lattice vector of layer l is given by $\mathbf{b}_j^{(\ell)} = R(\theta^{(\ell)})\mathbf{b}_j$, where $\mathbf{b}_1 = b(\sqrt{3}/2, -1/2)$ and $\mathbf{b}_2 = b(0, 1)$ with $b = 4\pi/(\sqrt{3}a)$. The Brillouin zone (BZ) corners are located at $\mathbf{K}_\xi^{(\ell)} = -\xi(2\mathbf{b}_1^{(\ell)} + \mathbf{b}_2^{(\ell)})/3$ where $\xi = \pm 1$ is the valley index.

The reciprocal lattice vectors of the moiré pattern 12 and 23 are defined by $\mathbf{G}_j^{\ell\ell'} = \mathbf{b}_j^{(\ell')} - \mathbf{b}_j^{(\ell)}$ where $(\ell, \ell') = (1, 2)$ and $(2, 3)$, respectively. Accordingly, the moiré lattice vectors in the real space are given by $\mathbf{G}_i^{\ell\ell'} \cdot \mathbf{L}_j^{\ell\ell'} = 2\pi\delta_{ij}$, and the corresponding moiré lattice period is written as $|\mathbf{L}_j^{\ell\ell'}| = 4\pi/(\sqrt{3}|\mathbf{G}_j^{\ell\ell'}|) = a/2 \sin(|\theta^{\ell\ell'}|/2)$. When \mathbf{G}_j^{12} and \mathbf{G}_j^{23} are close to each other, the interference of the two moiré patterns gives rise to a moiré-of-moiré pattern with reciprocal lattice vectors $\mathbf{G}_j = \mathbf{G}_j^{12} - \mathbf{G}_j^{23}$. We can define the associate periods \mathcal{L}_j in the real space.

In this paper, we consider trilayer systems where the two moiré patterns have a common periodicity for computational purposes. In this case, the period of the whole system can be expressed in terms of the individual moiré periods as [138]

$$\begin{aligned} \mathbf{L}_1 &= n\mathbf{L}_1^{12} + m\mathbf{L}_2^{12} = n'\mathbf{L}_1^{23} + m'\mathbf{L}_2^{23}, \\ \mathbf{L}_2 &= R(60^\circ)\mathbf{L}_1, \end{aligned} \quad (1)$$

with integers n, m, n' , and m' . Solving the above equation for the θ^{12} and θ^{23} , we obtain

$$\theta^{12} = \theta(n, m, n', m'), \quad \theta^{23} = -\theta(n', m', n, m), \quad (2)$$

where

$$\theta(n, m, n', m') = \tan^{-1} \frac{\sqrt{3} \{m(2n' + m') - (2n + m)m'\}}{(2n + m)(2n' + m') + 3mm' + (2n' + m')^2 + 3m'^2}. \quad (3)$$

Using the condition $\mathbf{G}_i \cdot \mathbf{L}_j = 2\pi\delta_{ij}$, the associated reciprocal lattice vectors are written as

$$\begin{aligned} \begin{pmatrix} \mathbf{G}_1 \\ \mathbf{G}_2 \end{pmatrix} &= \frac{1}{n^2 + nm + m^2} \begin{pmatrix} n + m & m \\ -m & n \end{pmatrix} \begin{pmatrix} \mathbf{G}_1^{12} \\ \mathbf{G}_2^{12} \end{pmatrix} \\ &= \frac{1}{n'^2 + n'm' + m'^2} \begin{pmatrix} n' + m' & m' \\ -m' & n' \end{pmatrix} \begin{pmatrix} \mathbf{G}_1^{23} \\ \mathbf{G}_2^{23} \end{pmatrix}. \end{aligned} \quad (4)$$

The lattice vectors \mathbf{L}_j of a commensurate double moiré lattice can always be written as an integer linear combination of the moiré-of-moiré interference periods, \mathcal{L}_j [145]. In the reciprocal space, accordingly, \mathbf{G}_j can be written as an integer linear combination of \mathbf{G}_i 's. In all the systems considered in the following, we have $\mathbf{L}_j = \mathcal{L}_j$ and $\mathbf{G}_j = \mathcal{G}_j$.

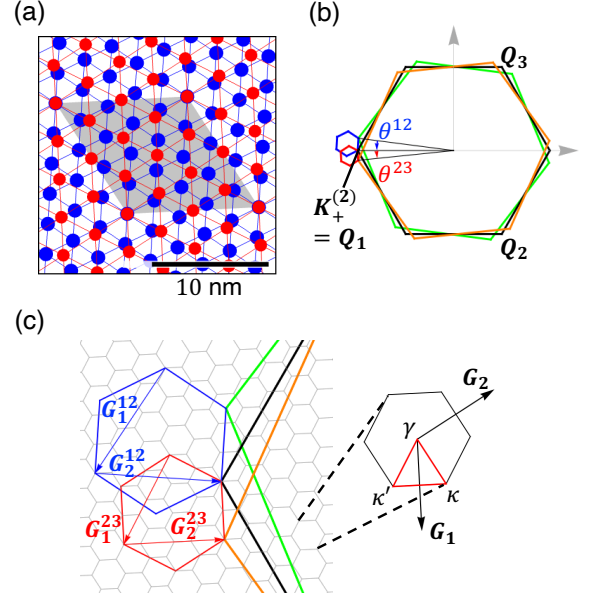


FIG. 3. A double-moiré system with a common periodicity, which is given by $(n, m, n', m') = (2, 3, 2, 2)$, corresponding to $(\theta^{12}, \theta^{23}) = (7.3^\circ, 5.8^\circ)$. (a) Real space structure of the non-relaxed moiré lattices 12 (blue) and 23 (red), where the vertexes represent MM stacking point. A gray rhombus is a common period (the moiré-of-moiré period). (b) Momentum space structure. Green, black, and orange hexagons represent the monolayer BZ of layer 1, 2, and 3 respectively, and blue and red hexagons are the BZs for the moiré 12 and 23. (c) A magnified view of the region around the K_+ -valley, where gray hexagons represent the BZ of the moiré-of-moiré pattern.

Figure 3 shows an example of such a double-moiré system with a common periodicity, which is given by $(n, m, n', m') = (2, 3, 2, 2)$, or $(\theta^{12}, \theta^{23}) = (7.3^\circ, 5.8^\circ)$. Figure 2(a) shows the real space structure of the moiré lattices 12 (blue) and 23 (red), with the common period is indicated by a gray rhombus. Figure 2(b) shows the corresponding k -space structure. Green, black, and orange hexagons represent the monolayer BZ of layer 1, 2, and 3 respectively, and blue and red hexagons are the BZs for the moiré 12 and 23. Figure 2(c) provides a magnified view of the region around the K_+ -valley, where gray hexagons represent the BZ of the common period, i.e., the moiré-of-moiré pattern.

For alternate twist cases with small twist angles, two moiré lattice vectors are nearly parallel, requiring a huge unit cell for commensuration of the two moiré periods. In this case, we neglect the tiny misorientation of the moiré lattice vectors \mathbf{L}_j^{12} and \mathbf{L}_j^{23} , while retaining their norms[138]. Under this approximation, the moiré-of-moiré commensurate period is expressed as

$$\mathbf{L}_1 = n\mathbf{L}_1^{12} = n'\mathbf{L}_1^{23}, \quad \mathbf{L}_2 = R(60^\circ)\mathbf{L}_1, \quad (5)$$

instead of Eqs. (1) and Eq. (2).

B. Continuum method for lattice relaxation

We compute the relaxed lattice structure of the trilayer TMD using a continuum method similar to that used for twisted graphene systems [138, 146, 147]. In this model, the lattice distortion is described by a displacement field $\mathbf{s}^{(\ell)}(\mathbf{r})$, which represents the shift of an atom on layer l at position \mathbf{r} . We treat $\mathbf{s}^{(\ell)}(\mathbf{r})$ as a smooth function in \mathbf{r} , assuming a long wavelength displacement where its spatial scale is much larger than the atomic lattice constant. We assume that the total structural energy is given by $U = U_E + U_B^{12} + U_B^{23}$ as a functional of $\mathbf{s}^{(\ell)}(\mathbf{r})$, where U_E is the elastic energy and $U_B^{\ell\ell'}$ is the interlayer binding energy of layers l and l' . Here U_E is written as [148, 149]

$$U_E = \sum_{l=1}^3 \frac{1}{2} \int \left[(\mu + \lambda) (s_{xx}^{(\ell)} + s_{yy}^{(\ell)})^2 + \mu \left\{ (s_{xx}^{(\ell)} - s_{yy}^{(\ell)})^2 + 4 (s_{xy}^{(\ell)})^2 \right\} \right] d^2\mathbf{r}, \quad (6)$$

where λ and μ are Lamé factors of monolayer TMD, and $s_{ij}^{(\ell)} = (\partial_i s_j^{(\ell)} + \partial_j s_i^{(\ell)})/2$ is the strain tensor. The interlayer binding energy of adjacent layers $(l, l') = (1, 2), (2, 3)$ is given by [146]

$$U_B^{\ell\ell'} = \int d^2\mathbf{r} \sum_{j=1}^3 2U_0 \cos \left[\mathbf{G}_j^{\ell\ell'} \cdot \mathbf{r} + \mathbf{b}_j \cdot (\mathbf{s}^{(\ell')} - \mathbf{s}^{(\ell)}) \right], \quad (7)$$

where $\mathbf{b}_3 = -\mathbf{b}_1 - \mathbf{b}_2$, $\mathbf{G}_3^{\ell\ell'} = -\mathbf{G}_1^{\ell\ell'} - \mathbf{G}_2^{\ell\ell'}$. We ignore the binding energy of layers 1 and 3, which is known to be relevant in small twist angles of the order of 0.1° [139, 150].

The parameters for WSe₂ are listed as $\lambda = 185.2$ eV/nm², $\mu = 302.2$ eV/nm² [91], and an interlayer potential strength of $U_0 = 0.07889$ eV/nm² [91]. The optimized lattice structure is numerically obtained by minimizing the lattice energy, $U = U_E + U_B^{12} + U_B^{23}$, with respect to $\mathbf{s}^{(\ell)}(\mathbf{r})$. The details of the numerical calculation used to obtain the optimized structure are presented in Appendix A.

C. Continuum Hamiltonian with lattice relaxation

We construct a continuum Hamiltonian of twisted trilayer TMD by extending that for twisted bilayers [56, 59, 72, 73, 75, 77] and including the effect of the lattice relaxation. By using the basis of the valence band around K_ξ point, it is give by a 3×3 matrix,

$$H^{(\xi)} = \begin{pmatrix} H_1(\mathbf{k}) + \Delta_+^{12} & \Delta_T^{12,*} & \\ \Delta_T^{12} & H_2(\mathbf{k}) + \Delta_-^{12} + \Delta_+^{23} & \Delta_T^{23,*} \\ & \Delta_T^{23} & H_3(\mathbf{k}) + \Delta_-^{23} \end{pmatrix}, \quad (8)$$

where the ℓ -th component corresponds to layer ℓ . We neglect the remote hopping between layer 1 and layer 3. Here H_ℓ is the valence band Hamiltonian for monolayer TMD of the layer ℓ , given by

$$H_\ell = -\frac{\hbar^2}{2m^*} \left(\mathbf{k} + \frac{e}{\hbar} \mathbf{A}^{(\ell)} \right)^2 + \delta (s_{xx}^{(\ell)} + s_{yy}^{(\ell)}) + \frac{\hbar^2}{2m^*} \alpha \left(k_+ + \frac{e}{\hbar} A_+^{(\ell)} \right) (s_{xx}^{(\ell)} + s_{yy}^{(\ell)}) \left(k_- + \frac{e}{\hbar} A_-^{(\ell)} \right), \quad (9)$$

where $\mathbf{k} = (k_x, k_y)$ is a momentum vector, $s_{\mu\nu}^{(\ell)} = (\partial_\mu s_\nu^{(\ell)} + \partial_\nu s_\mu^{(\ell)})/2$ is the strain tensor, $\mathbf{A}^{(\ell)}$ is the effective vector potential due to the distortion, given by

$$\mathbf{A}^{(\ell)} = \xi \frac{\hbar}{ea} \beta \left(s_{xx}^{(\ell)} - s_{yy}^{(\ell)}, -2s_{xy}^{(\ell)} \right), \quad (10)$$

and we used the notation $k_\pm = \xi k_x \pm i k_y$ and $A_\pm = \xi A_x \pm i A_y$. For the parameters, we take $\alpha = -1.83$ eV, $\beta = 1.99$ eV and $\delta = -2.24$ eV [151], and $m^* = 0.43m_e$ [59, 152, 153] for WSe₂, where m_e is the bare electron mass. The Hamiltonian of monolayer TMD including the strain effect [Eq. (9)] is derived by projecting the 2×2 version [151] to the valence band by the second perturbation [See Appendix B].

The $\Delta_\pm^{\ell\ell'}(\mathbf{r})$ is the intralayer potential by the moiré pattern $\ell\ell'$, and it is given by

$$\Delta_\pm^{\ell\ell'}(\mathbf{r}) = 2V \sum_{j=1}^3 \cos \left[\mathbf{G}_j^{\ell\ell'} \cdot \mathbf{r} + \mathbf{b}_j \cdot (\mathbf{s}^{(\ell')} - \mathbf{s}^{(\ell)}) \pm \psi \right], \quad (11)$$

where \pm correspond to the layer ℓ and ℓ' . The $\Delta_T^{\ell\ell'}(\mathbf{r})$ is the interlayer hopping term between layers ℓ and ℓ' , and is written as

$$\Delta_T^{\ell\ell'}(\mathbf{r}) = w \sum_{j=1}^3 e^{i\mathbf{q}_j^{\ell\ell'} \cdot \mathbf{r} + i\mathbf{Q}_j \cdot (\mathbf{s}^{(\ell')} - \mathbf{s}^{(\ell)})}, \quad (12)$$

where

$$\begin{aligned} \mathbf{q}_1^{\ell\ell'} &= \mathbf{K}_\xi^{(\ell)} - \mathbf{K}_\xi^{(\ell')}, \\ \mathbf{q}_2^{\ell\ell'} &= \mathbf{q}_1^{\ell\ell'} + \xi \mathbf{G}_1^{\ell\ell'}, \\ \mathbf{q}_3^{\ell\ell'} &= \mathbf{q}_1^{\ell\ell'} + \xi \left(\mathbf{G}_1^{\ell\ell'} + \mathbf{G}_2^{\ell\ell'} \right), \end{aligned} \quad (13)$$

and

$$\mathbf{Q}_1 = \mathbf{K}_\xi, \quad \mathbf{Q}_2 = \mathbf{Q}_1 + \xi \mathbf{b}_1, \quad \mathbf{Q}_3 = \mathbf{Q}_1 + \xi (\mathbf{b}_1 + \mathbf{b}_2). \quad (14)$$

The parameters V , w and ψ in Eqs. (11) and (12) are determined from the DFT calculation for the non-twist bilayer WSe₂ with different lateral shifts, as detailed in Appendix. C. The obtained values are listed as $V = 5.966$ meV, $w = 14.32$ meV, $\psi = 77.02^\circ$.

For the intralayer potential Eq. (11), the relationship between $\Delta_+^{\ell\ell'}$ and $\Delta_-^{\ell\ell'}$ depends on the parameter ψ : we

have $\Delta_+^{\ell\ell'} = \Delta_-^{\ell\ell'}$ for $\psi = 0$, and $\Delta_+^{\ell\ell'} = -\Delta_-^{\ell\ell'}$ for $\psi = 90^\circ$. For $\psi = 77^\circ$ in the current model, we have an approximate relationship $\Delta_+^{\ell\ell'} \approx -\Delta_-^{\ell\ell'}$. For the later convenience, we also define $V_\ell(\mathbf{r})$ as the intralayer potential term of layer l in the diagonal blocks of Eq. (8), i.e.,

$$V_1(\mathbf{r}) = \Delta_+^{12}, \quad V_2(\mathbf{r}) = \Delta_-^{12} + \Delta_+^{23}, \quad V_3(\mathbf{r}) = \Delta_-^{23}. \quad (15)$$

For the current choice of ψ , V_2 is nearly equal to $-V_1 - V_3$, because $\Delta_-^{\ell\ell'} \approx -\Delta_+^{\ell\ell'}$.

The numerical calculation goes as follows. The Hamiltonian of Eq. (8) hybridizes a set of wavenumbers $\mathbf{k} = \mathbf{k}_0 + \mathbf{G}$, where $\mathbf{G} = n_1 \mathbf{G}_1 + n_2 \mathbf{G}_2$ (n_1, n_2 : integer) are reciprocal vectors of the moiré-of-moiré period [Eq. (4)], and \mathbf{k}_0 is a wavenumber within the moiré-of-moiré BZ. To obtain the low-energy spectrum, we truncate the high-momentum components and retain only the wavenumbers with $|\mathbf{G}| \leq 4 \max(|\mathbf{G}_j^{12}|, |\mathbf{G}_j^{23}|)$. We construct the Hamiltonian matrix within the finite set of wavenumbers, and obtain energy bands by plotting its eigenvalue as a function of \mathbf{k}_0 .

While out-of-plane lattice distortion is neglected in the structural relaxation, real moiré TMD systems exhibit corrugated structures, where the interlayer spacing is larger in the MM regions than in the MX/XM regions [91, 154]. In the electronic band calculations, the effect of corrugation is partially incorporated into the DFT-based band parameters v , w , and ψ , as the structural optimization (including interlayer distance) was performed for non-twisted bilayers with MM, MX, and XM stackings [Appendix C].

III. HELICAL TRILAYERS

A. Commensurate helical trilayers

First, we consider a commensurate helical trilayer TMD, where the two moiré patterns share the exact same periodicity, as seen in the $\alpha\alpha$, $\alpha\beta$, and $\beta\alpha$ stackings shown in Fig. 2(c). Such a structure can be obtained by starting from an equal-angle trilayer with $\theta^{12} = \theta^{23}$ and slightly expanding the atomic period of the middle layer to align the orientations of moiré 12 and moiré 23 (i.e., $\mathbf{G}_j^{12} = \mathbf{G}_j^{23}$) [60, 115, 138].

The interlayer stacking energy of the commensurate trilayer depends on the relative shift between the two moiré lattices. Similar to twisted trilayer graphene [138], the lowest energy state is achieved in the $\alpha\beta$ and $\beta\alpha$ structures, where the MM points of moiré 12 and moiré 23 repel each other. The stability of the $\alpha\beta$ and $\beta\alpha$ domains can be understood as a result of frustration in the local relaxation of the middle layer [138]. Here, we perform the band calculations for relaxed commensurate trilayers of $\alpha\beta$ and $\beta\alpha$ stacking, with $\theta^{12} = \theta^{23} = 1^\circ$. In Fig. 4, the upper panels present the results for the $\alpha\beta$ case, showing (a) the energy bands near the valence band top, along with the layer-projected density

of states (DOS), (b) the intralayer potential maps V_1 , V_2 , and V_3 [Eq. (15)], and (c) the real-space distribution of wavefunctions in representative bands, averaged over the Brillouin zone. Here we labeled the bands as $\alpha\beta 1, \alpha\beta 2, \alpha\beta 3, \dots$ in descending order from the top. The lower panels [Figs. 4 (d), (e) and (f)] show the corresponding figures for the $\beta\alpha$ case.

In this system, the interlayer hopping terms $\Delta_T^{12}, \Delta_T^{23}$ are significantly suppressed by the lattice relaxation [see, Appendix D], so the electronic states are primarily governed by the intralayer potential terms, V_1, V_2, V_3 . The potential of the outer layers, V_1 and V_3 , are similar to that of a moiré bilayer, where $V_1 (V_3)$ take the maxima and minima at the XM (MX) and MX (XM) domains, respectively [91, 155–157]. These domains are not perfect triangles but exhibit convex and concave shapes, and this deformation can be attributed to the interaction between moiré 12 and moiré 23 through the middle layer [138]. The second-layer potential V_2 is approximately given by $-V_1 - V_3$ as argued in the previous section, and therefore that V_2 has an energy range approximately twice as large as that of V_1 and V_3 .

In the $\alpha\beta$ structure, the potential maxima of V_1 at XM and those of V_3 at MX coincide in position (XMX), and hence the minima of $V_2 \approx -V_1 - V_3$ form a triangular lattice. In contrast, the minima of V_1 (MX) and V_3 (XM) are located at different positions within the moiré unit cell, occupying different sublattices of a honeycomb lattice. As a result, the maxima of V_2 appear at the midpoints of these sublattices (MXM), forming a Kagome lattice. The situation is also illustrated in a schematic diagram in Fig. 1. The potential map of $\beta\alpha$ is nearly identical to that of $\alpha\beta$ but inverted along the energy axis. Thus, in $\beta\alpha$, the roles of the Kagome and triangular lattices for V_2 are reversed, with its minima forming a Kagome lattice and its maxima forming a triangular lattice. The inverted profiles in $\alpha\beta$ and $\beta\alpha$ can be explained using Eq. (11), considering that $\mathbf{G}_j^{\ell\ell'}$ and $\mathbf{s}^{(\ell)}$ have opposite signs, and that $\psi = 77^\circ$ is close to $\pi/2$.

The energy bands strongly reflect the structure of the potential maps of V_1, V_2, V_3 . In the energy spectrum, states in the upper energy region ($E \gtrsim 20$ meV) are predominantly localized on layer 2 due to the high potential energy of V_2 . In the $\alpha\beta$ structure, the energy bands in this region correspond to states bound to the maxima of V_2 , which form a Kagome lattice. As a result, a characteristic Kagome band structure emerges, including a flat band ($\alpha\beta 3$) with a wavefunction following the Kagome pattern. The band $\alpha\beta 6$ and $\alpha\beta 7$ are bound states at the maxima of V_1 and V_3 , which are arranged in a shared trigonal lattice. While the overall band structures are primarily determined by the intralayer potentials V_ℓ , additional features arise from the strain-induced effective vector potentials $\mathbf{A}^{(\ell)}$ [Eq.(10)] and the interlayer hopping terms $\Delta_T^{(\ell\ell')}$ [Eq.(12)]. In the absence of both contributions, the flat band $\alpha\beta 3$ is attached to the topmost graphene-like band cluster. Including these terms shifts the flat band downward toward the lower dispersive bands. They are

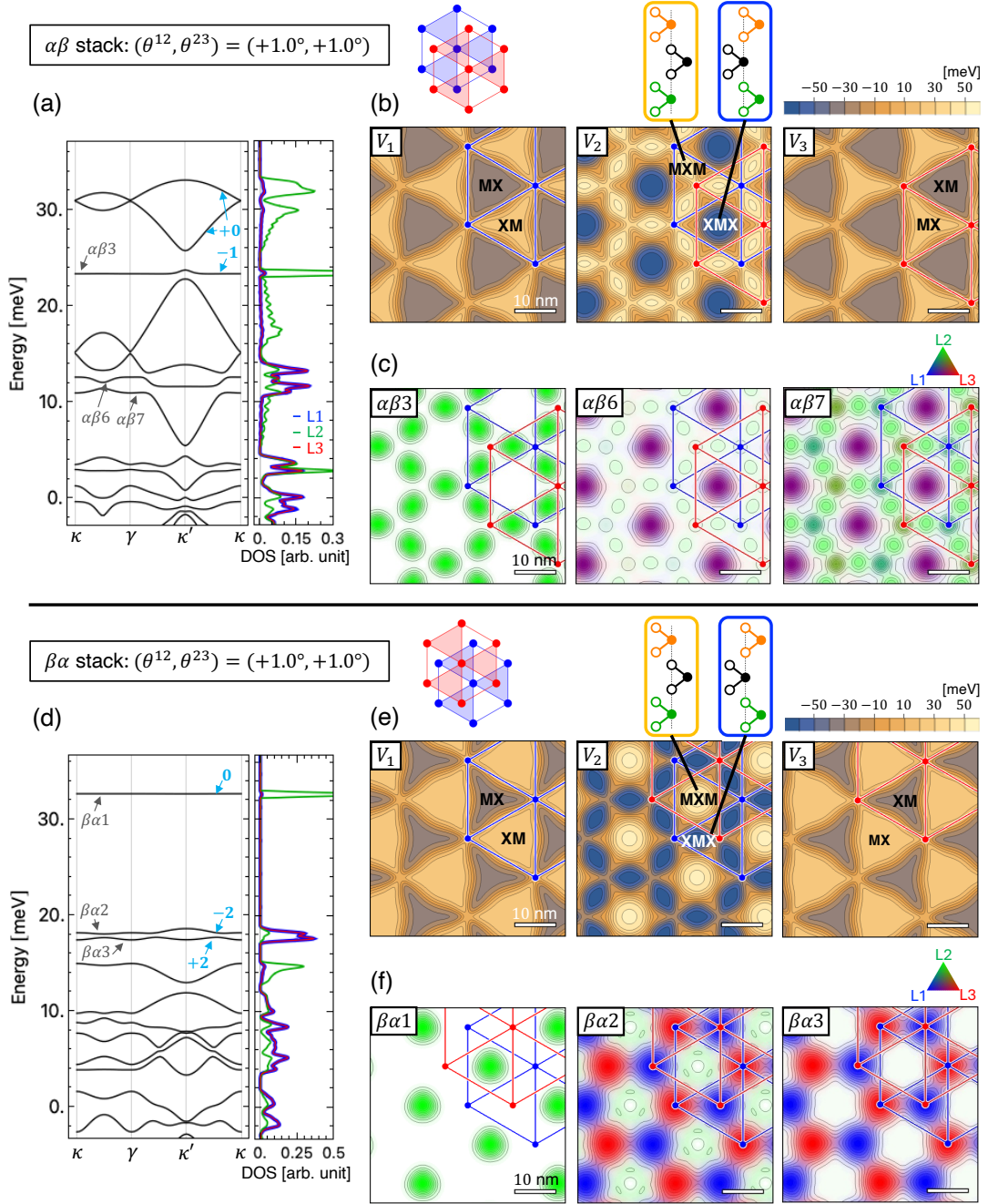


FIG. 4. (a) Band structure and the layer-projected DOS near the valence band edge for a relaxed $\alpha\beta$ -stacked twist trilayer WSe₂ with $(\theta^{12}, \theta^{23}) = (1.0^\circ, 1.0^\circ)$. Blue numbers by the bands indicate the Chern number of the K_+ valley. (b) Contour maps of the intralayer potential V_1, V_2, V_3 . Blue and red lattices represent moiré lattices of 12 and 23, respectively. (c) Real-space distribution of wavefunctions for representative bands, averaged over the Brillouin zone. The colors indicate the layer distribution, as shown in the triangular diagram in the inset. (d-f) Corresponding figures for a commensurate $\beta\alpha$ -stacked trilayer with $(\theta^{12}, \theta^{23}) = (1.0^\circ, 1.0^\circ)$.

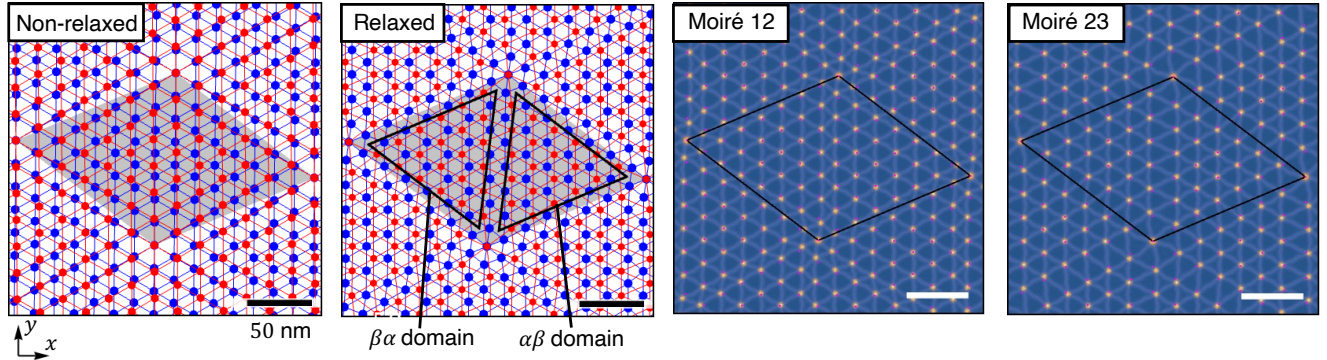
also responsible for opening a small gap between the flat and dispersive bands and for generating a non-zero valley Chern number.

In the $\beta\alpha$ structure, the inverted potential results in a completely distinct energy band structure. The maxima

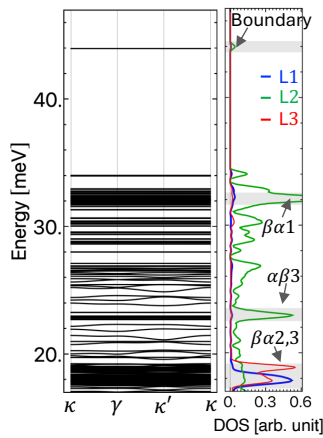
of V_2 form a triangular pattern, giving rise to the $\beta\alpha 1$ state. The maxima of V_1 and V_3 do not share the center position but instead form a hexagonal lattice. The bands $\beta\alpha 2$ and $\beta\alpha 3$ are bound states at these potential maxima, where layers 1 and 3 serve as different sublattices of a

$$(\theta^{12}, \theta^{23}) = (+1.07^\circ, +0.93^\circ)$$

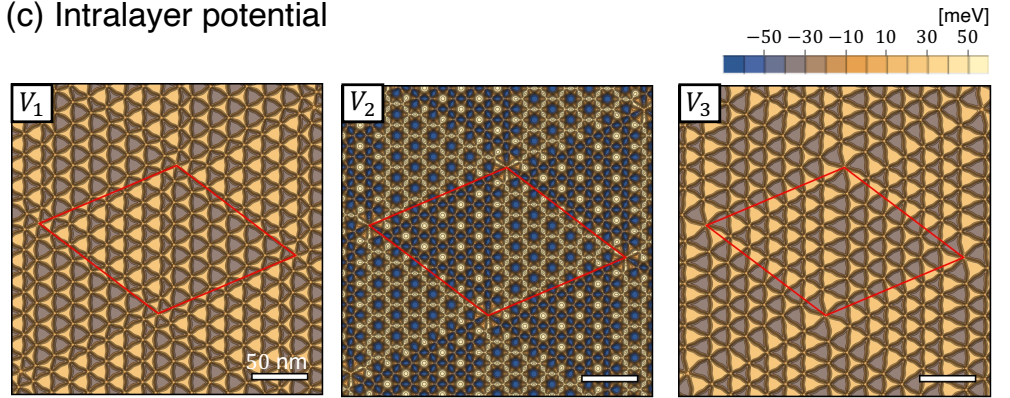
(a) Moiré structure



(b) Band structure



(c) Intralayer potential



(d) Wave function

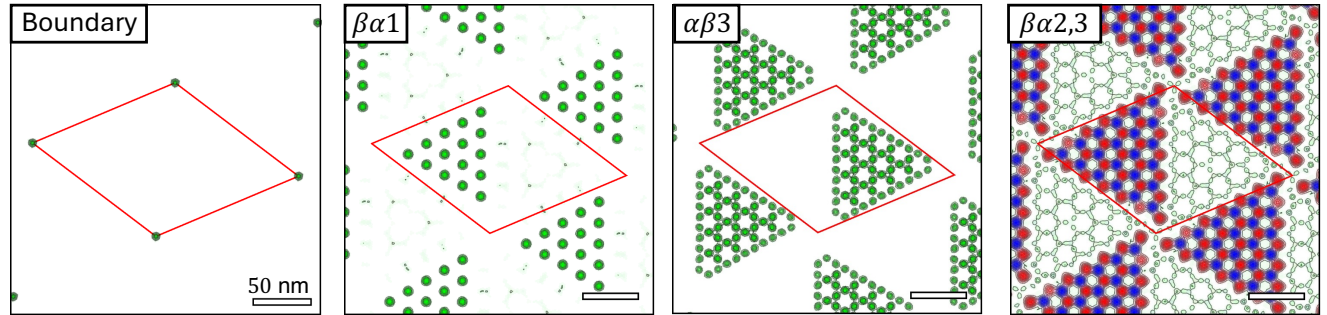


FIG. 5. (a) Structural relaxation in a helical twist trilayer WSe_2 with $(\theta^{12}, \theta^{23}) = (1.07^\circ, 0.93^\circ)$. The left two panels present schematic illustrations of the double moiré lattice for non-relaxed and relaxed cases, where blue and red dots represent MM stacking points of moiré 12 and moiré 23, respectively. A gray rhombus represents a moiré-of-moiré unit cell. The right two panels plot the interlayer binding energy U_B^{12} and U_B^{23} in the relaxed structure, where bright and dark regions correspond to MM and MX/XM stacking, respectively. Small magenta dots indicate the MM stacking without lattice relaxation. (b) Band structure and layer-resolved density of states (DOS) of the same system. (c) Contour maps of the intralayer potentials V_1, V_2, V_3 . (d) Real-space distribution of representative wavefunctions, averaged over the shaded energy regions in the DOS plot of (b). The colors indicate the layer distribution.

honeycomb lattice, as seen in Fig. 4(f). The corresponding energy bands in Fig. 4(d) have small dispersions and Chern numbers of ± 2 , which can presumably be captured by a Haldane-type model based on a honeycomb lattice [158–160].

B. General helical trilayers

Now we consider a general helical trilayer TMD, where the two moiré patterns have different periodicities. Here we calculate the relaxed structure and the electronic band structure of the helical twist trilayer WSe₂ with $(\theta^{12}, \theta^{23}) = (1.07^\circ, 0.93^\circ)$, which corresponds to $(n, m, n', m') = (1, 7, 1, 6)$ in Eq. (2). Figure 5(a) summarizes the optimized lattice structure. The left two panels show the moiré pattern before (left) and after (right) lattice relaxation, where blue and red dots indicate the MM stacking of moiré 12 and moiré 23, respectively. The right two panels plot the local binding energy U_B^{12} and U_B^{23} in the relaxed structure, where the bright and dark regions correspond to the MM and MX/XM stacking. In each of moiré 12 and 23, the MM stacking points shrink, while the MX and XM regions expand to form a triangular domains as in moiré bilayer. In the moiré-of-moiré scale, MM stacking points of moiré 12 and those of 23 avoid each other, leading to the emergence of commensurate moiré domains of $\alpha\beta$ and $\beta\alpha$ argued above.

Figure 5(b) shows the band structure and the layer-projected DOS near the valence band top of the relaxed trilayer. Figure 5(c) presents the intralayer potential V_1, V_2 and V_3 . Figure 5(d) illustrates the real-space distribution of the wave functions corresponding to representative peaks in (b). Here, we take the average of the squared wave amplitude over the states within the shaded region in (b), with the color representing the layer distribution as defined in the inset.

Notably, the DOS in the original moiré-of-moiré trilayer in Fig. 5(b) shows reasonable agreement with the sum of DOS for $\alpha\beta$ and $\beta\alpha$ commensurate trilayers [Figs. 4 (a) and (c)]. In particular, the peaks labeled by $\beta\alpha 1, \beta\alpha 2, \beta\alpha 3$ and $\alpha\beta 3$ in Fig. 5(b) correspond to the flat bands with the same labels in the commensurate band structure. We also see that the corresponding wavefunctions shown in Fig. 5(d) share the same spatial distributions of the local-band wavefunctions in Figs. 4(b) and (d). These states are mainly distributed in either of $\alpha\beta$ or $\beta\alpha$ domains with a small inter-domain connection, leading to nearly flat dispersions in the moiré-of-moiré energy bands.

On the other hand, there are also bands that do not correspond to the $\alpha\beta/\beta\alpha$ domain states. Specifically, the topmost band is located at a higher energy (~ 42 meV) than the highest bands of $\alpha\beta/\beta\alpha$, separated by the rest of the spectrum by an energy gap. This band is associated with boundary states, which are sharply localized at the corners (MMM positions) of the moiré-of-moiré domains, as shown in Figure 5(d). These modes can be understood

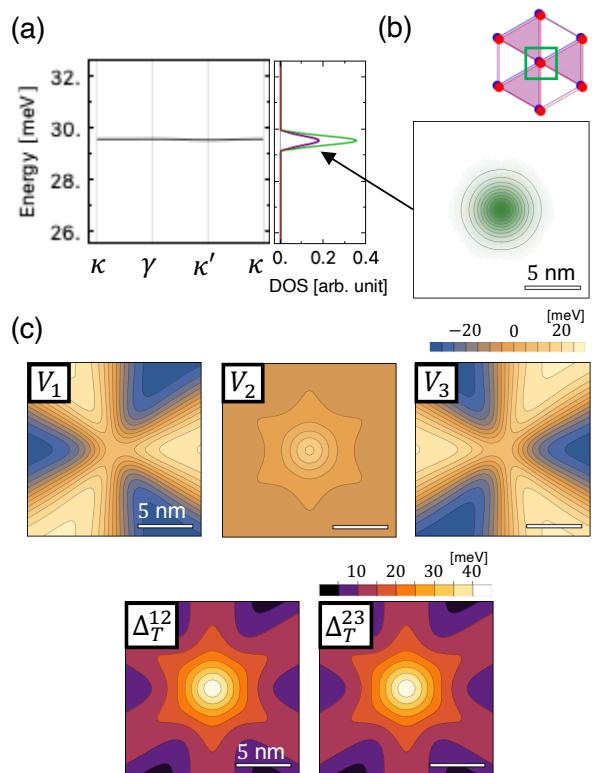


FIG. 6. (a) The topmost valence band and its projected density of states (DOS) in a relaxed helical twist trilayer WSe₂ with local $\alpha\alpha$ stacking for $(\theta^{12}, \theta^{23}) = (1.0^\circ, 1.0^\circ)$. (b) Real-space distribution of the topmost band around the MMM stacking region, corresponding to the area enclosed by a green rectangle in the schematic figure above. The color scheme follows Fig. 4. (c) Contour maps of intralayer potentials V_1, V_2, V_3 and the absolute values of the interlayer hopping terms $|\Delta_T^{12}|, |\Delta_T^{23}|$.

by considering the electronic structure of a commensurate $\alpha\alpha$ trilayer, which has a MMM stack at the corners. Figure 6 shows the result of the band calculation for $\alpha\alpha$ trilayer with $(\theta^{12}, \theta^{23}) = (1.0^\circ, 1.0^\circ)$. Here we show (a) the energy band of the MMM corner mode, (b) its wave function, and (c) the intralayer potential V_1, V_2, V_3 and the interlayer hopping amplitudes $|\Delta_T^{12}|, |\Delta_T^{23}|$ in the vicinity of the MMM corner. We see that the interlayer hopping $|\Delta_T^{12}|, |\Delta_T^{23}|$ peaks at the corner with a greater magnitude than the V_i terms, and consequently, the MMM corner hosts a localized state bound by the dominant interlayer hopping. This MMM bound state qualitatively explains the corner state observed in Fig. 5(b), although its energy does not match precisely due to discrepancies in the strain-induced terms in the Hamiltonian.

We note that these boundary states are not topologically-protected corner states, as they are fragile under a lateral shift between the moiré patterns, which remove the MMM stacking. In real twist trilayers, the two moiré patterns do not form exact commensuration

within the moiré-of-moiré cell unlike the assumed structures in this calculation. As a result, the domain corners can adopt different local moiré configurations depending on the lateral shift, leading to corner-dependent variations in the boundary states.

The size of the $\alpha\beta$ and $\beta\alpha$ domains increases as the two twist angles approach each other. In the case of equal angles, $\theta^{12} = \theta^{23} = \theta$, the moiré-of-moiré period is given by $\mathcal{L} = (4\pi/\sqrt{3})|\mathbf{G}_j^{12} - \mathbf{G}_j^{23}| = a/4\sin^2(\theta/2)$. The period becomes $0.8 \mu\text{m}$ at $\theta = 1.0^\circ$ and decreases further as θ becomes smaller. Therefore, it is in principle possible to fabricate a periodic Kagome potential over a scale on the order of micrometers.

IV. ALTERNATE TWIST TRILAYERS

A. Commensurate alternate trilayers

Alternate twist trilayers ($\theta_{12} \cdot \theta_{23} < 0$) have fundamentally distinct electronic properties. First, we consider a commensurate alternate trilayer with $\theta^{12} = -\theta^{23}$, where the moiré 12 and 23 have the exactly same period. The total structural energy depends on the lateral shift of the two moiré lattices, the most stable registry is $\alpha\alpha'$ structure [Fig. 2(g)] where the MM stacking points of moiré 12 and those of 23 are overlapped. The underlying mechanism of domain formation is essentially the same as in alternate twisted trilayer graphene [138]. Here we calculate the energy bands for a relaxed twisted trilayer WSe₂ with $(\theta^{12}, \theta^{23}) = (1^\circ, -1^\circ)$ with $\alpha\alpha'$ stacking. Figure 7 shows the energy bands, the intralayer potential map and the wave functions. The V_1 and V_3 plotted in Fig. 7(b) are equivalent to the intralayer potential of twisted bilayer, where $V_1(V_3)$ take the maxima and minima in triangular XM (MX) and MX (XM) domains, respectively. In contrast to the helical case, V_1 and V_3 are exactly identical due to the mirror symmetry with respect to the middle layer. Therefore, the middle layer potential, $V_2 \approx -V_1 - V_3$, is simply twice as deep as V_1 and V_3 , leading to an array of trigonal potential wells with a depth about 100 meV.

The topmost bands $\alpha\alpha'1, 2, 3$ originate from bound states at the maxima of the triangular potential well of V_2 . The $\alpha\alpha'1$ corresponds to an s -like orbital, which is compactly localized in the well, resulting in an exponentially small band dispersion. The $\alpha\alpha'2$ and $\alpha\alpha'3$ states originate from p -like orbitals with broader spatial distributions, resulting in bandwidths of a few meV. These two bands correspond to bound states with opposite angular momenta $l_z = \pm 1$, which correspond to the eigenstate $e^{2\pi i l_z/3}$ in C_3 rotation. The energy splitting between $l_z = \pm 1$ arises from a strain-induced effective magnetic field. As the twist angle decreases, the potential well widens in space, causing $\alpha\alpha'2$ and $\alpha\alpha'3$ to become more localized. Simultaneously, higher bound states $\alpha\alpha'4, \alpha\alpha'5, \dots$ emerge. Note that in twisted TMD bilayers, the potential wells have only half the depth,

leading to fewer bound states compared to a trilayer with the same twist angle.

B. General alternate trilayers

As a representative example of general alternate trilayers, we consider a trilayer WSe₂ with $(\theta^{12}, \theta^{23}) = (1.10^\circ, -0.88^\circ)$, which corresponds to $(n, n') = (5, -4)$ in Eq. (5). Figure 8(a) shows the optimized lattice structure presented with the same figure arrangement as in Fig. 5(a) for the helical case. By comparing the non-relaxed and relaxed cases, we observe that lattice relaxation induces locally commensurate $\alpha\alpha'$ domains arranged in a hexagonal pattern, along with domain boundaries. The energy band, the intralayer potential, and representative wavefunctions are presented in Fig. 8(b), (c) and (d), respectively. In the potential map [Fig. 8(c)], $\alpha\alpha'$ domains accommodate an array of triangular quantum well discussed above.

In the energy spectrum [Fig. 8(b)], $\alpha\alpha'1, 2, 3$ bands appear as peaks at the corresponding energy, with an identical wave distribution as shown in Fig. 8(d). We can also see a bunch of boundary modes which do not correspond to $\alpha\alpha'$ domain states. The peaks between $\alpha\alpha'1$ and $\alpha\alpha'2, 3$ are the modes localized around the corners of the $\alpha\alpha'$ domain, where the intralayer potential has different well structure [Fig. 8(c)] from the $\alpha\alpha'$ domain. As previously noted in the helical case, the moiré configurations near domain boundaries are highly sensitive to the relative periodicities of the moiré patterns, resulting in variations in the boundary states.

V. EFFECTS OF PERPENDICULAR ELECTRIC FIELD

By applying a perpendicular electric field, we can control the layer polarization by modulating the electrostatic potential of each layer. This also allows us to tune the hybridization of energy bands across layers, enabling the formation of diverse electronic structures composed of s - and p -like orbitals localized in triangular dots.

The effect of a vertical electric field can be introduced by adding a term to the Hamiltonian [Eq. (8)],

$$H_E = \begin{pmatrix} -\Delta_E & \\ & 0 \\ & & \Delta_E \end{pmatrix}, \quad (16)$$

where Δ_E is the electrostatic potential difference between adjacent layers.

Figure 9 summarizes the electric field dependence of the electronic structure of the $\alpha\alpha'$ -stacked twisted trilayer WSe₂ with $(\theta^{12}, \theta^{23}) = (+1.0^\circ, -1.0^\circ)$. Figure 9(a) presents a density map of the layer-projected DOS, plotted as a function of the electric field (Δ_E) and energy. The $\Delta_E = 0$ corresponds to the energy bands in Fig. 7. The right panel shows a schematic diagram illustrating the

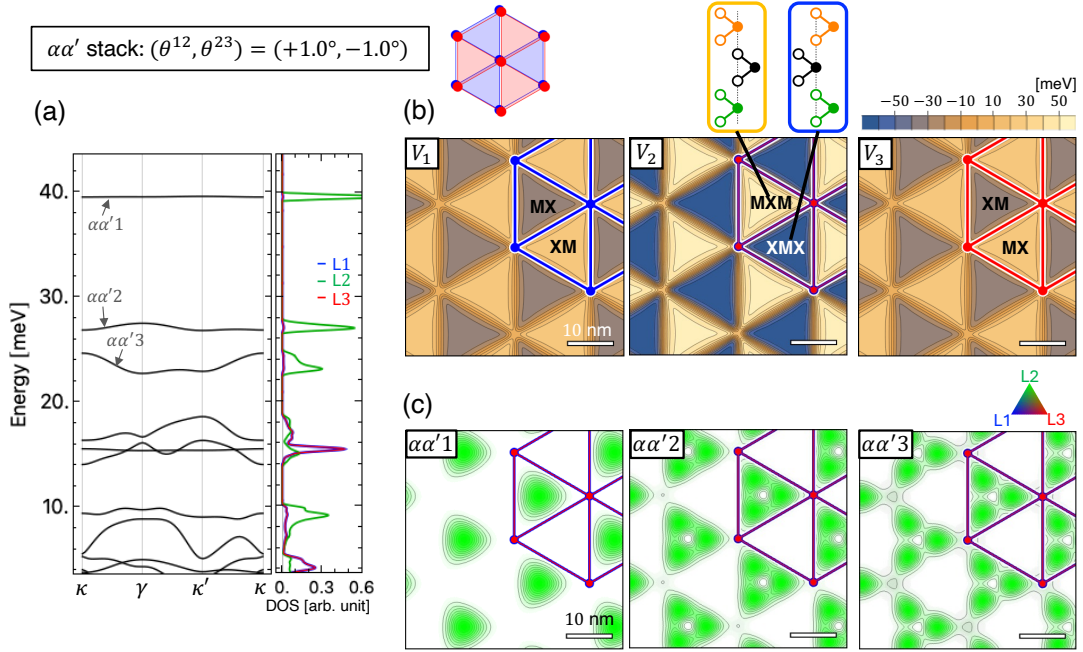


FIG. 7. (a) Band structure near the valence band edge, (b) contour maps of the intralayer potential, and (c) wavefunctions of representative bands, calculated for a relaxed $\alpha\alpha'$ twisted trilayer WSe₂ with $(\theta^{12}, \theta^{23}) = (1.0^\circ, -1.0^\circ)$. The results are plotted in a similar manner to Fig. 4.

energies of localized orbitals; for example, $L2s$ denotes the s -like bound state localized in a triangular quantum well in layer 2. With increasing Δ_E , we clearly observe that the bands originating from layer 3 (red) shift upward in energy and eventually surpass those of layer 2 (green), while the bands from layer 1 (blue) move downward.

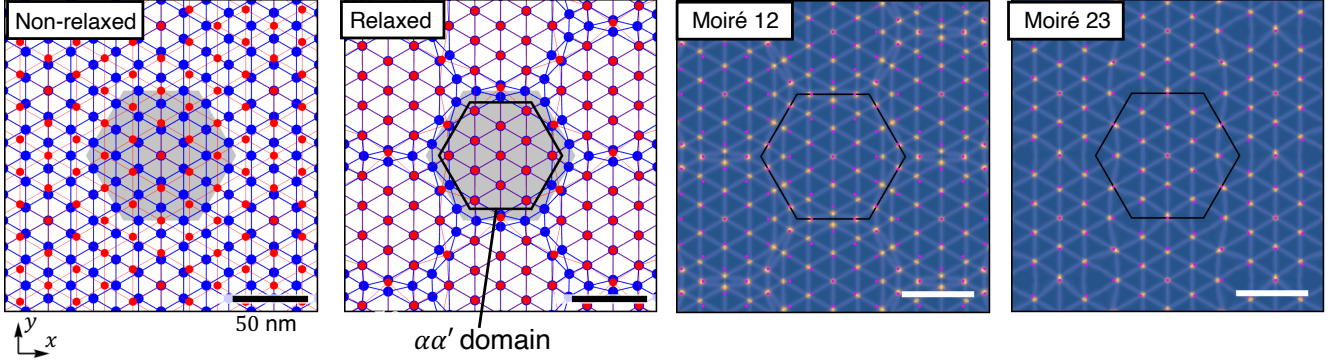
At the crossing points of orbital energies from different layers, we observe significant band hybridization and anticrossing behavior. Figures 9(b–d) show the band structure and representative wavefunctions near the crossings labeled (b), (c), and (d) in Fig. 9(a). Panel (b) corresponds to the intersection of $L2s$ and $L3s$, where the s -like states from layers 2 and 3 form a honeycomb lattice, resulting in a graphene-like band structure. In this system, Δ_E effectively acts as the Dirac mass. Likewise, the crossing point (c) gives rise to a honeycomb lattice formed by p orbitals. At $\Delta_E = 20$ meV, in particular, we observe a characteristic structure where a Dirac cone and a flat band coexist, resembling the $S = 1$ Dirac band [161–166]. At point (d), an unusual situation arises where s and p orbitals occupy different sublattices of a honeycomb lattice. In this case, we observe quadratic band touching at $\Delta_E = 10$ meV and 12 meV. These characteristic features can be captured by simple tight-binding models of s and/or p orbitals on a honeycomb lattice, as discussed in Appendix E. We also observe that the subbands often carry non-zero valley Chern numbers $C_K = -C_{K'}$. In the effective s/p tight-binding model, this behavior can be attributed to the effect of the strain-induced effective magnetic field.

At large Δ_E , the electronic states near the valence band top are fully polarized on layer 3, where interlayer hybridization is absent [Fig. 9(a)]. Nonetheless, non-trivial band structures still emerge due to the interplay between different orbitals within the same layer. Figure 10 shows the band structure near the valence band top for $\Delta_E = 60, 150$ and 300 meV. The topmost band originates from an s -orbital, and the second and third bands from p -orbitals (with $l_z = \pm 1$), with all orbitals arranged on a triangular lattice. The three lower bands, enclosed by the dashed yellow rectangle, stem from the orbitals which we refer to as d -orbitals for convenience. In an isolated triangular quantum well, these correspond to a single orbital with angular momentum $l_z = 0$ and a doubly-degenerate set with $l_z = \pm 1$, which happen to be nearly degenerate in energy. The d -bands exhibit a characteristic structure, where a flat band is sandwiched between massive Dirac bands. At large Δ_E , where interlayer hybridization is negligible, the Dirac mass becomes smaller, leading to an approximate triple degeneracy with the flat band at the band touching point. This characteristic band structure is well reproduced by an effective tight-binding model for d -orbitals, as discussed in Appendix E. For lower twist angles, we can find energy bands related with even higher orbitals of triangular well.

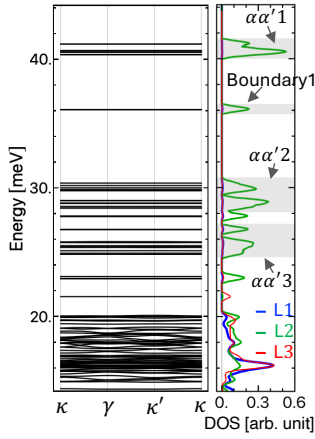
The band structures in the $\alpha\beta$ and $\beta\alpha$ stackings can also be modulated by applying a perpendicular electric field. In the $\alpha\beta$ case, for example, the Kagome band localized on layer 2 can hybridize with s - or p -like orbitals on the triangular lattices of layers 1 and 3, depending on

$$(\theta^{12}, \theta^{23}) = (+1.10^\circ, -0.88^\circ)$$

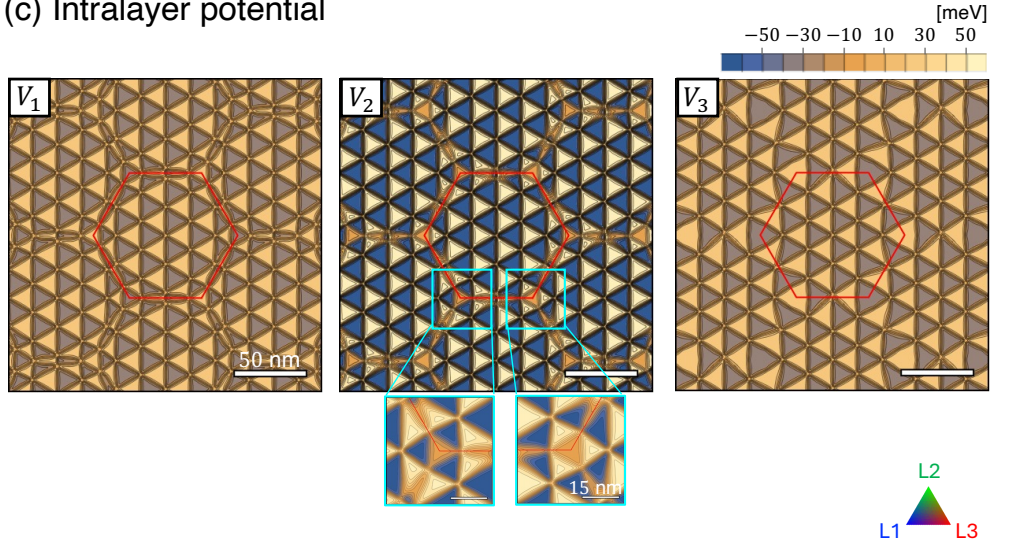
(a) Moiré structure



(b) Band structure



(c) Intralayer potential



(d) Wave function

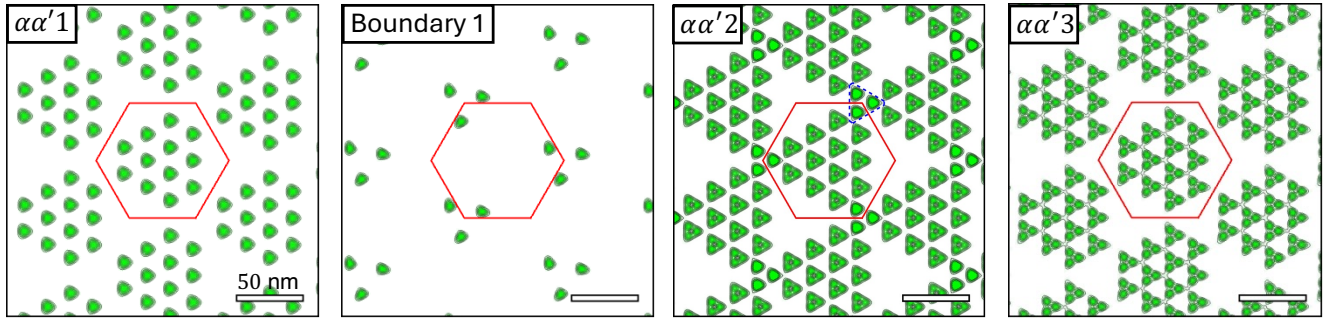


FIG. 8. (a) Structural relaxation, (b) band structure, (c) contour maps of the intralayer potentials, and (d) wavefunctions averaged over representative energy regions, calculated for an alternate twist trilayer WSe₂ with $(\theta^{12}, \theta^{23}) = (1.10^\circ, -0.88^\circ)$. The results are plotted in a similar manner to Fig. 5.

the field strength. For the $\beta\alpha$ stacking, the electric field allows for hybridization among s/p orbitals residing on three distinct triangular lattices associated with layers 1, 2, and 3. Further details of these calculations are presented in Appendix F

Although we performed the band calculation above

using the lattice structure optimized at $\Delta_E = 0$, the vertical electric field generally affects the relaxed lattice structure. In twisted bilayer TMD, the MX and XM regions have opposite electric polarizations along z direction [95, 167–169], and consequently, a perpendicular electric field modifies the relative sizes of these

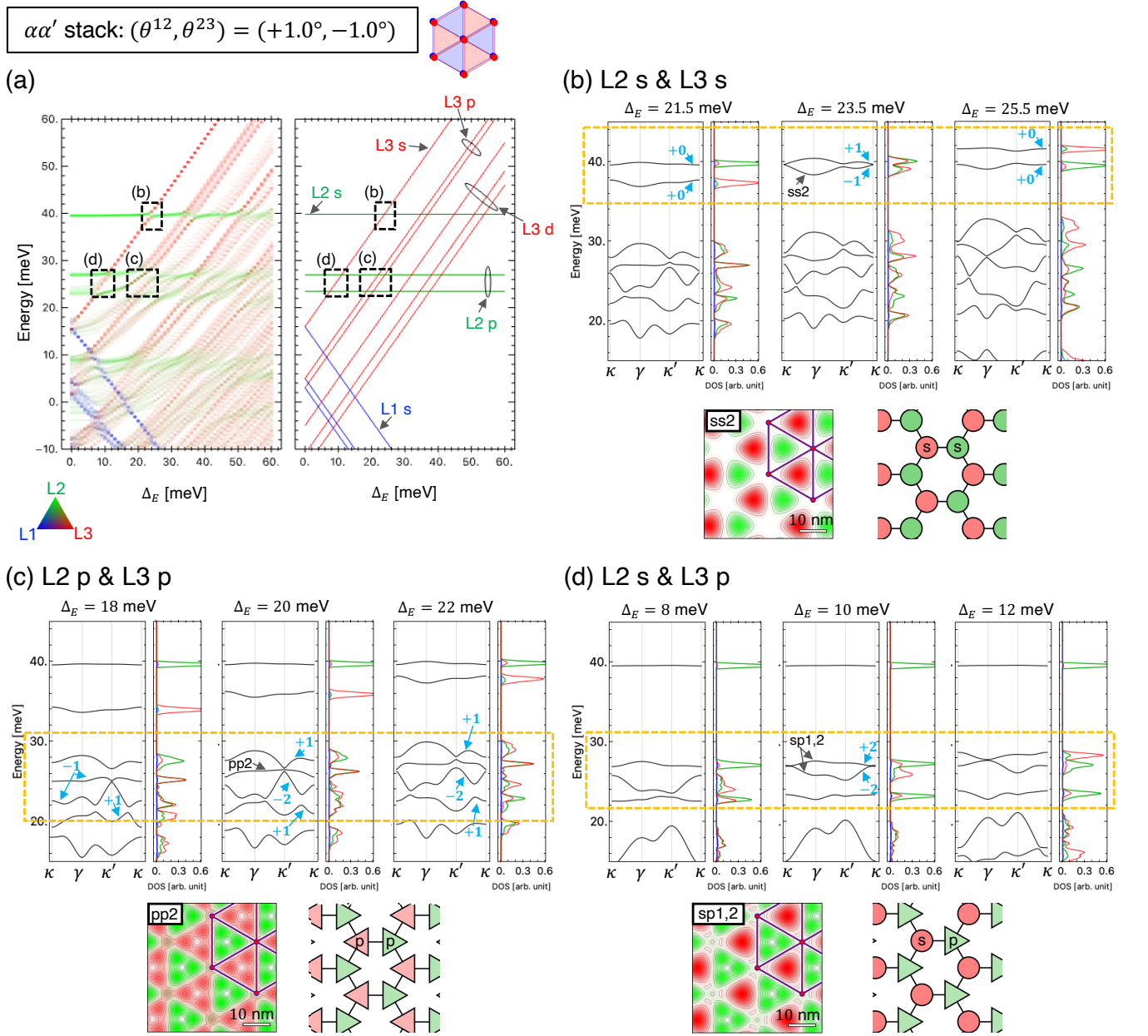


FIG. 9. (a) Density map of the layer-projected density of states (DOS) for the $\alpha\alpha'$ -stacked twisted trilayer WSe₂ with $(\theta^{12}, \theta^{23}) = (+1.0^\circ, -1.0^\circ)$. The horizontal and vertical axes represent the electric field Δ_E and energy, respectively. The right panel presents a schematic diagram illustrating the energies of localized orbitals. (b) Energy band structure in the region labeled (b) in Fig.9(a). The bottom panels show the BZ-averaged wavefunction of a representative band, labeled *ss2* (left), and the corresponding effective lattice (right). (c,d) Band structures and representative wavefunctions for the crossing points labeled (c) and (d) in Fig.9(a). The color schemes follow those in Fig. 4.

domains.[96] In a twist angle around $\sim 1^\circ$, such a modulation becomes significant in an electric field range of Δ_E exceeding a few eV [96], which is much larger than the values considered above. We expect relevant effects to occur in moderate electric fields in marginal twisted trilayers with $\theta \sim \mathcal{O}(0.1^\circ)$, which we leave for future studies.

VI. CONCLUSION

We have conducted a systematic theoretical study on the structural and electronic properties of twisted trilayer WSe₂, revealing distinct behaviors arising from the interplay of two independent moiré patterns. As in twisted trilayer graphene, lattice relaxation plays a crucial role in domain formation: helical trilayers develop $\alpha\beta$ and $\beta\alpha$

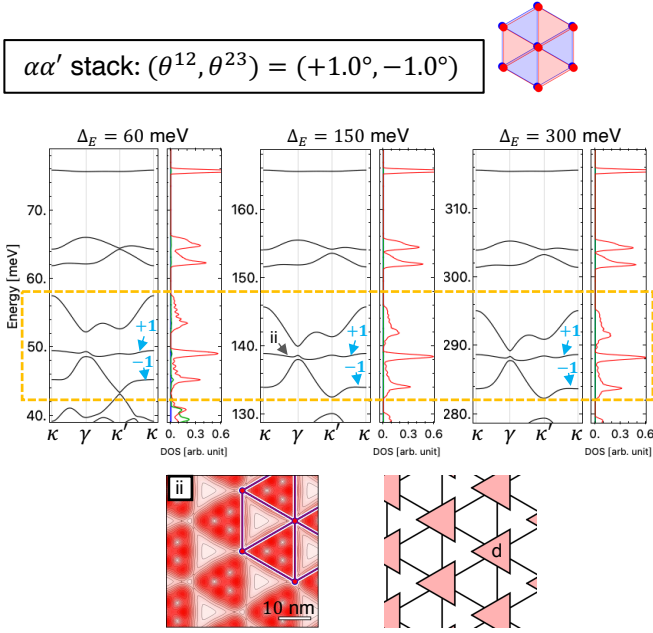


FIG. 10. (Top) Band structures near the valence band top of the $\alpha\alpha'$ -stacked twisted trilayer WSe_2 with $(\theta^{12}, \theta^{23}) = (+1.0^\circ, -1.0^\circ)$, under electric fields $\Delta_E = 60, 150,$ and 300 meV. (Bottom left) Density plot of the wavefunction for the flat band labeled ii at $\Delta_E = 150$ meV, averaged over the Brillouin zone. (Bottom right) Schematic illustration of the corresponding effective triangular lattice model.

domains where the two moiré lattices shift to minimize overlap, while alternating trilayers stabilize $\alpha\alpha'$ domains where the two moiré lattices align. A key feature unique to trilayer TMD systems is the summation of moiré potentials from the outer layers onto the middle layer, effectively doubling its potential depth. This mechanism leads to qualitatively distinct electronic structures compared to bilayer systems. In helical trilayers, a Kagome lattice potential naturally emerges in $\alpha\beta$ domains, producing localized flat bands that could host strongly correlated states. In alternating trilayers, the deeper triangular potential wells provide stronger confinement than in twisted bilayers. The global electronic spectrum reflects a combination of bulk-like states from commensurate domains and isolated boundary modes localized at domain intersections.

Furthermore, we have demonstrated that the layer polarization of valence states can be controlled by a vertical electric field, introducing an additional degree of tunability to trilayer moiré systems. In particular, electric field modulation enables hybridization between orbitals localized on different layers, allowing for the engineering of novel electronic band structures, including Dirac bands, flat bands, and their coexistence.

Our findings highlight the significance of moiré potential summation as a design principle in twisted multilayer structures, offering an expanded platform for engineering

moiré-based quantum phenomena beyond bilayer TMDs. Future research directions include investigating the effects of external perturbations, many-body interactions, and optical responses in these trilayer moiré systems.

ACKNOWLEDGMENTS

We thank Kazunari Matsuda, Young-Woo Son, and Manato Fujimoto for the discussions and suggestion about this work. This work was supported in part by JSPS KAKENHI Grant Number JP20H01840, JP21H05236, JP21H05232, JP25K00938 and by JST CREST Grant Number JPMJCR20T3, Japan.

Appendix A: Numerical method for lattice relaxation

Here, we derive the self-consistent equation for the structural relaxation from the Euler-Lagrange equation for the total energy $U = U_E + U_B^{12} + U_B^{23}$ [See, Sec. II B], following the method adopted in the previous paper [138]. First, we introduce

$$\begin{aligned} \mathbf{w} &= \mathbf{s}^{(1)} + \mathbf{s}^{(2)} + \mathbf{s}^{(3)} \\ \mathbf{u} &= \mathbf{s}^{(1)} - 2\mathbf{s}^{(2)} + \mathbf{s}^{(3)} \\ \mathbf{v} &= \mathbf{s}^{(1)} - \mathbf{s}^{(3)}, \end{aligned} \quad (\text{A1})$$

and rewrite U as a functional of \mathbf{w}, \mathbf{u} and \mathbf{v} . Here \mathbf{w} represents an overall translation of three layers, while \mathbf{u} and \mathbf{v} are relative sliding which are mirror-even and odd, respectively, with respect to the layer 2. In the subsequent analysis, we set $\mathbf{w} = \mathbf{0}$ and focus solely on \mathbf{u} and \mathbf{v} , as \mathbf{w} does not alter the interlayer registration and therefore does not impact the formation of moiré domains.

We assume $\mathbf{s}^{(\ell)}$ (so \mathbf{u} and \mathbf{v}) are periodic in the original moiré-of-moiré period, and define the Fourier components as

$$\mathbf{u}(\mathbf{r}) = \sum_{\mathbf{G}} \mathbf{u}_{\mathbf{G}} e^{i\mathbf{G}\cdot\mathbf{r}}, \quad \mathbf{v}(\mathbf{r}) = \sum_{\mathbf{G}} \mathbf{v}_{\mathbf{G}} e^{i\mathbf{G}\cdot\mathbf{r}}, \quad (\text{A2})$$

where $\mathbf{G} = m_1\mathbf{G}_1 + m_2\mathbf{G}_2$ are the moiré-of-moiré reciprocal lattice vectors.

The Euler-Lagrange equations are written as

$$\begin{aligned} \mathbf{u}_{\mathbf{G}} &= -6V_0 \sum_{j=1}^3 \left(f_{\mathbf{G},j}^{12} + f_{\mathbf{G},j}^{23} \right) \hat{K}_{\mathbf{G}}^{-1} \mathbf{b}_j, \\ \mathbf{v}_{\mathbf{G}} &= -2V_0 \sum_{j=1}^3 \left(f_{\mathbf{G},j}^{12} - f_{\mathbf{G},j}^{23} \right) \hat{K}_{\mathbf{G}}^{-1} \mathbf{b}_j, \end{aligned} \quad (\text{A3})$$

where

$$\hat{K}_{\mathbf{G}} = \begin{pmatrix} (\lambda + 2\mu) G_x^2 + \mu G_y^2 & (\lambda + \mu) G_x G_y \\ (\lambda + \mu) G_x G_y & (\lambda + 2\mu) G_y^2 + \mu G_x^2 \end{pmatrix}, \quad (\text{A4})$$

and

$$\begin{aligned}\sin\left[\mathbf{G}_j^{12}\cdot\mathbf{r}-\mathbf{b}_j\cdot(\mathbf{u}+\mathbf{v})/2\right]&=\sum_{\mathbf{G}}f_{\mathbf{G},j}^{12}e^{i\mathbf{G}\cdot\mathbf{r}}, \\ \sin\left[\mathbf{G}_j^{23}\cdot\mathbf{r}+\mathbf{b}_j\cdot(\mathbf{u}-\mathbf{v})/2\right]&=\sum_{\mathbf{G}}f_{\mathbf{G},j}^{23}e^{i\mathbf{G}\cdot\mathbf{r}}.\end{aligned}\quad (\text{A5})$$

We obtain the optimized $\mathbf{u}_{\mathbf{G}}$ and $\mathbf{v}_{\mathbf{G}}$ by solving Eq. (A2) and (A3) self-consistently. We assume that the relaxation preserves the symmetries of the model C_{3z} . Furthermore, We only take a finite number of the Fourier components in $|\mathbf{G}| < 4 \max(|n|, |m|, |n'|, |m'|) |G_j|$, which is sufficient to consider the lattice relaxation of the systems considered in this work.

In this scheme, the $\mathbf{G} = 0$ component of $\mathbf{s}^{(\ell)}$, which corresponds to a uniform translation of layer ℓ , cannot be optimized directly due to $\hat{\mathbf{K}}_{\mathbf{G}=0} = 0$ in Eq. (A3). These components should instead be treated as parameters, and the optimized structure can then be determined by comparing the total energies of self-consistent solutions obtained for different choices of $\mathbf{s}_{\mathbf{G}=0}^{(\ell)}$. For commensurate trilayers where the moiré 12 and 23 share the same periodicity (i.e., $\mathbf{G}_j^{12} = \mathbf{G}_j^{23}$), the total energy significantly depends on $\mathbf{s}_{\mathbf{G}=0}^{(\ell)}$. In the case of helical trilayers, the energetically favored structures are the $\alpha\beta$ and $\beta\alpha$ stackings, which are realized by setting $\mathbf{s}_{\mathbf{G}=0}^{(3)} = \pm(\mathbf{a}_1^{(3)} + \mathbf{a}_2^{(3)})/3$ and $\mathbf{s}_{\mathbf{G}=0}^{(1)} = \mathbf{s}_{\mathbf{G}=0}^{(2)} = \mathbf{0}$. For the alternate trilayers, the lowest-energy configuration is the $\alpha\alpha'$ stacking, achieved when all layers are unshifted $\mathbf{s}_{\mathbf{G}=0}^{(\ell)} = \mathbf{0}$ for all $\ell = 1, 2, 3$. For general trilayers $\mathbf{G}_j^{12} \neq \mathbf{G}_j^{23}$, the total energy does not sensitively depend on the $\mathbf{G} = 0$ components because of a large moiré-of-moiré period, so we primarily show the case with no lateral shift $\mathbf{s}_{\mathbf{G}=0}^{(\ell)} = \mathbf{0}$.

Appendix B: Effective Hamiltonian for strained monolayer TMD

We derive an effective valence-band Hamiltonian for a monolayer TMD in the presence of lattice distortion. We assume the system has the only in-plane lattice distortion specified the displacement vector $\mathbf{s}(\mathbf{r})$.

In the basis of the conduction and valence band (ψ_c, ψ_v), the effective Hamiltonian at valley $\xi = \pm$ is given by [151]

$$H^\xi = F_0\sigma_0 + F_z\sigma_z + \mathbf{F}\cdot\boldsymbol{\sigma}, \quad (\text{B1})$$

where σ_μ is the Pauli matrix, σ_0 is the 2×2 identity matrix. The F_i are defined by

$$\begin{aligned}F_0 &= f_0 + f_3 \sum_{\mu=x,y} s_{\mu\mu}, \\ F_z &= f_1 + f_4 \sum_{\mu=x,y} s_{\mu\mu}, \\ \mathbf{F} &= (F_x, F_y) = f_2a \left(\mathbf{k} + \frac{e}{\hbar}\mathbf{A} \right),\end{aligned}\quad (\text{B2})$$

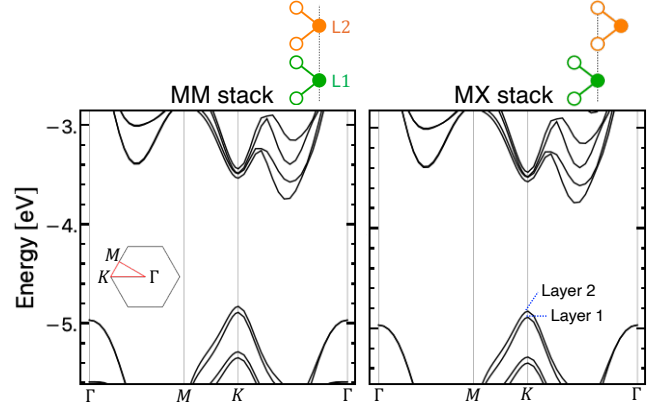


FIG. 11. DFT band calculation of the non-twist bilayer WSe₂ for MM and MX stacking. Hexagon in the left panel shows the Brillouin zone of bilayer WSe₂, where red line represents the k-space path we took in the DFT calculation. Right top figures of each panel are atomic arrangement of each stacking, where green and orange correspond to the layer 1 and 2 respectively.

where $s_{\mu\nu} = (\partial_\mu s_\nu + \partial_\nu s_\mu)/2$ is the tensor strain, $\mathbf{A} = \xi(\hbar f_5)/(ef_2a)(s_{xx} - s_{yy}, -2s_{xy})$ is the effective vector potential, and f_j are the material dependent parameters [151]. Here we ignore the second order terms in $s_{\mu\nu}$.

We derive the effective Hamiltonian projected onto the valence band by the second order perturbation as follows.

$$\begin{aligned}H_V^\xi &= (F_0 - F_z) + \begin{pmatrix} 2F_z & F_- \\ F_+ & 0 \end{pmatrix}, \\ \rightarrow H_V^\xi &\simeq (F_0 - F_z) - F_+ (2F_z)^{-1} F_-, \end{aligned}\quad (\text{B3})$$

where $F_\pm = F_x \pm iF_y$. By using Eq. (B2), it is explicitly written as

$$\begin{aligned}H_V^\xi &= (f_0 - f_1) + (f_3 - f_4) \sum_{\mu=x,y} s_{\mu\mu} - \frac{\hbar^2}{2m^*} \left(\mathbf{k} + \frac{e}{\hbar}\mathbf{A} \right)^2 \\ &+ \frac{\hbar^2}{2m^*} \left(\frac{f_4}{f_1} \right) \left(k_+ + \frac{e}{\hbar}A_+ \right) \left(\sum_{\mu=x,y} s_{\mu\mu} \right) \left(k_- + \frac{e}{\hbar}A_- \right),\end{aligned}\quad (\text{B4})$$

where $m^* = (\hbar^2 f_1)/(f_2a)^2$ is the effective mass.

Appendix C: Determining Parameters for the Continuum Model

We determine the parameters V , w and ψ of continuum Hamiltonian for twisted bilayer TMDs based on DFT calculations [56, 59, 72, 73, 75, 77]. First, we perform the DFT band calculation for non-twist bilayer TMDs with MM, MX and XM stacking, which correspond to inter-layer lateral shift vector $\mathbf{d} = \mathbf{0}$ and $\pm(\mathbf{a}_1 + \mathbf{a}_2)/3$, respectively. For each case, we obtain the $k \cdot p$ Hamiltonian

at near K point to fit the DFT band structure and then determine the parameters to reproduce the valence band structure.

We performed density functional theory (DFT) calculations for non-twisted bilayer WSe₂ by using Vienna Ab initio Simulation Package (VASP)[170, 171], with the Perdew-Burke-Ernzerhof (PBE) generalized gradient approximation (GGA)[172] and DFT-D3 method of Grimme with zero-damping function[173]. The spin-orbit-coupling effects are included self-consistently[174]. Plane wave cutoff energy was set to 335 eV. We sampled the $11 \times 11 \times 1$ grid of k points for the Brillouin-zone by Gamma centered mesh. In z direction, a vacuum layer thicker than 25 Å is introduced to eliminate interactions across supercells. We shift the top layer in parallel relative to the bottom layer over 6×6 grid in the unit cell and calculated 21 symmetrically unique shifted bilayers. The interlayer distance of each laterally shifted bilayer configuration is optimized to the value that minimizes the total energy.

Fig. 11 is the DFT band structure of bilayer TMD with MM and MX stacking. To compare the calculation of the different stackings, we take the vacuum energy as the zero energy. Here, the vacuum energy can be calculated as a planar average potential at the center of the vacuum layer. The first and second valence bands at the K -point are split by $\Delta E_K^{MM} = 85.91$ meV and $\Delta E_K^{MX} = 60.4$ meV for MM and MX stackings, respectively. The valence band tops of MM and MX stackings differ by $E_{K,1st}^{MM} - E_{K,1st}^{MX} = 25.20$ meV. The first and second valence band states in MX stacking are predominantly polarized to layer 2 and layer 1, respectively.

We define the effective valence-band Hamiltonian of TMD bilayer at K point as [56, 59, 72, 73, 75, 77]

$$H_K = \begin{pmatrix} \Delta_+(\mathbf{d}) & \Delta_T^*(\mathbf{d}) \\ \Delta_T(\mathbf{d}) & \Delta_-(\mathbf{d}) \end{pmatrix}, \quad (\text{C1})$$

where

$$\Delta_T(\mathbf{d}) = w \left[1 + e^{b_1 \cdot \mathbf{d}} + e^{(b_1 + b_2) \cdot \mathbf{d}} \right], \quad (\text{C2})$$

and

$$\Delta_{\pm}(\mathbf{d}) = 2V \sum_{j=1}^3 \cos[\mathbf{b}_j \cdot \mathbf{d} \pm \psi]. \quad (\text{C3})$$

Here we take the valence band of layer 1 and 2 as the basis $(\psi^{(1)}, \psi^{(2)})$. The parameters (w, V, ψ) are determined by fitting to ΔE_K^{MM} , ΔE_K^{MX} , $E_{K,1st}^{MM} - E_{K,1st}^{MX}$, and the layerwise polarization in MM and MX stackings in the DFT calculation. The resulting parameters are $(w, V, \psi) = (14.32 \text{ meV}, 5.966 \text{ meV}, 77.02^\circ)$.

Appendix D: Impact of lattice relaxation on electronic structure

The lattice relaxation plays a significant role in the electronic structures of trilayer TMD Figure 12 com-

pare the band structure and the moiré potentials in non-relaxed (left) and relaxed (right) $\alpha\beta$ -stacked twist trilayer WSe₂ with $(\theta^{12}, \theta^{23}) = (1.0^\circ, 1.0^\circ)$. In each figure, the left panels shows the band structure and layer-resolved DOS, and the right figures display the middle-layer intralayer potential V_2 and the interlayer hopping Δ_T^{12} (between layer 1 and 2). We observe that, in the non-relaxed case, the potential V_2 exhibits a honeycomb-like pattern, in contrast to the kagome lattice structure seen in the relaxed case. As discussed in the main text, the kagome potential arises from the overlap of triangular potentials V_1 and V_3 , each featuring flat tops/bottoms and sharply defined boundaries. Without lattice relaxation, however, these individual potentials become smoother and less distinct, causing the kagome structure to dissolve into a simpler hexagonal pattern.

The energy band structure is sensitively dependent on this change. The flat band comprising a Kagome band in the relaxed case is significantly moved downward in the non-relaxed case, and it can be interpreted as a flat band in p_x - p_y honeycomb lattice [175–177]. We also observe that The projected DOS for the non-relaxed case shows that the states around Fermi energy are only weakly localized at layer 2 compared to the relaxed case. This occurs because the interlayer hopping Δ_T^{12} is significantly suppressed by lattice relaxation as shown in Figure 12.

The energy band structures of other stackings, $\beta\alpha$ and $\alpha\alpha'$, are also affected by lattice relaxation. Figure 13 compares the band structures of these stackings with and without relaxation. Similar to the $\alpha\beta$ case, lattice relaxation greatly enhances the layer polarization, primarily due to the suppression of interlayer hopping. In the $\beta\alpha$ stacking, the band dispersion is significantly reduced as the triangular potential pockets deepen through relaxation.

Appendix E: The effective model for hybridized electron state under the electric field

In this section, we introduce effective models that qualitatively capture the field-tunable $s/p/d$ -hybridized electron states in the $\alpha\alpha'$ TMD trilayer [Fig. 9, Sec. V].

1. p-p honeycomb model

We first consider the energy bands highlighted in Fig. 9(c). These can be effectively modeled by a honeycomb lattice composed of p -orbitals, denoted as $|X, p_{\pm}\rangle$, where $X = A, B$ indicates the sublattice, and \pm labels the eigenstates of the C_{3z} rotation symmetry. Specifically, the C_{3z} operation acts as $C_{3z} |X, p_{\pm}\rangle = \omega^{\pm 1} |X, p_{\pm}\rangle$, with $\omega = \exp(i2\pi/3)$. Figure 14(a) shows a schematic illustration of the lattice structure with orbital $|X, p_{\pm}\rangle$, where the numbers at each corner indicate the phase of the orbital wave function. We define the primitive lattice vectors $\mathbf{a}_j = R(\pi(j-1)/3)(0, -1)$ for $(j = 1, \dots, 6)$,

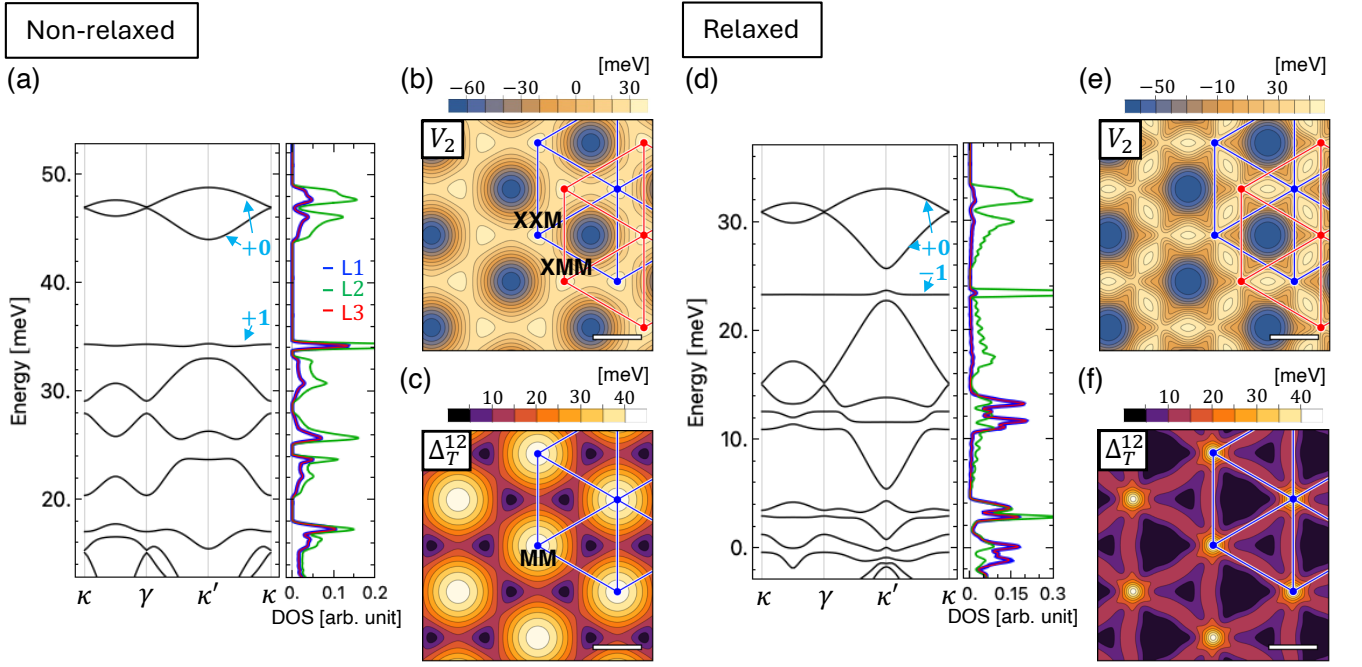


FIG. 12. (a) Band structure and the layer-projected DOS near the valence band edge for non-relaxed $\alpha\beta$ -stacked twist trilayer WSe₂ with helical twist angles, $(\theta^{12}, \theta^{23}) = (+1.0^\circ, +1.0^\circ)$. (b,c) Contour plot of (b) the intralayer potential of middle layer V_2 and (c) the absolute value of the interlayer hopping of moiré 12 $|\Delta_T^{12}|$ for non-relaxed case. (d-f) Similar plots for the relaxed twisted trilayer WSe₂, also shown in Fig. 4(a) and (b). The white scale bar represents 10 nm.

and also vectors connecting an A site to three neighboring B sites, $\tau_1 = (1/\sqrt{3}, 0)$, $\tau_2 = (-1/(2\sqrt{3}), 1/2)$, and $\tau_3 = (-1/(2\sqrt{3}), -1/2)$.

The Hamiltonian is written in the basis $(|Ap_+\rangle, |Ap_-\rangle, |Bp_+\rangle, |Bp_-\rangle)$ as

$$H_{pp} = \begin{pmatrix} E_{A+} + h_{A+} & h_{A-,A+}^* & u_{B+,A+}^* & u_{B-,A+}^* \\ h_{A-,A+} & E_{A-} + h_{A-} & u_{B+,A-}^* & u_{B-,A-}^* \\ u_{B+,A+} & u_{B+,A-} & E_{B+} + h_{B+} & h_{B-,B+}^* \\ u_{B-,A+} & u_{B-,A-} & h_{B-,B+} & E_{B-} + h_{B-} \end{pmatrix}. \quad (\text{E1})$$

Here $u_{B\mu,Av}$ ($\mu, \nu = \pm$) is the nearest-neighbor hopping term from A to B sublattice, given by

$$u_{B+,A+}(\mathbf{k}) = u_{B-,A-}(\mathbf{k}) \quad (\text{E2}) \\ = t_{pp}^{AB} \left(-e^{-i\mathbf{k}\cdot\tau_1} - e^{-i\mathbf{k}\cdot\tau_2} - e^{-i\mathbf{k}\cdot\tau_3} \right),$$

$$u_{B-,A+}(\mathbf{k}) = t_{pp}^{AB} \sum_{j=1}^3 2\omega^{j-1} e^{-i\mathbf{k}\cdot\tau_j}, \\ u_{B+,A-}(\mathbf{k}) = (\omega \leftrightarrow \omega^* \text{ in } u_{B-,A+}), \quad (\text{E3})$$

where we assume that the hopping integral between neighboring A and B sites is proportional to a summation of the phase differences at the two shared corners. The $h_{A\pm}$, $h_{B\pm}$, $h_{A+,A-}$ and $h_{B+,B-}$, are the next nearest-neighbor hopping terms between the same sublattices,

defined by

$$h_{A+}(\mathbf{k}) = h_{B-}(\mathbf{k}) \\ = t_{pp}^{AA/BB} \left[\sum_{j=1,3,5} \omega e^{-i\mathbf{k}\cdot\mathbf{a}_j} + \sum_{j=2,4,6} \omega^* e^{-i\mathbf{k}\cdot\mathbf{a}_j} \right], \\ h_{A-}(\mathbf{k}) = h_{B+}(\mathbf{k}) \\ = t_{pp}^{AA/BB} \left[\sum_{j=1,3,5} \omega^* e^{-i\mathbf{k}\cdot\mathbf{a}_j} + \sum_{j=2,4,6} \omega e^{-i\mathbf{k}\cdot\mathbf{a}_j} \right], \quad (\text{E4})$$

and

$$h_{A-,A+}(\mathbf{k}) = h_{B-,B+}(\mathbf{k}) \\ = t_{pp}^{AA/BB} \left[\left(e^{-i\mathbf{k}\cdot\mathbf{a}_1} + e^{-i\mathbf{k}\cdot\mathbf{a}_4} \right) \right. \\ \left. + \omega^* \left(e^{-i\mathbf{k}\cdot\mathbf{a}_2} + e^{-i\mathbf{k}\cdot\mathbf{a}_5} \right) + \omega \left(e^{-i\mathbf{k}\cdot\mathbf{a}_3} + e^{-i\mathbf{k}\cdot\mathbf{a}_6} \right) \right].$$

$E_{A\pm}$ and $E_{B\pm}$ are the constant on-site energy given by

$$E_{A\pm} = E_A \pm \Delta h_A / 2 \\ E_{B\pm} = E_B \pm \Delta h_B / 2. \quad (\text{E5})$$

Noting that the A and B sublattices correspond to layer 3 and layer 2, respectively, in the original calculation of Sec. V, E_A and E_B represent the on-site energies of the layers under a perpendicular electric field, where $E_A - E_B$ corresponds to Δ_E . Δh_A and Δh_B describe the orbital Zeeman splitting of p_{\pm} orbitals due to the strain-induced

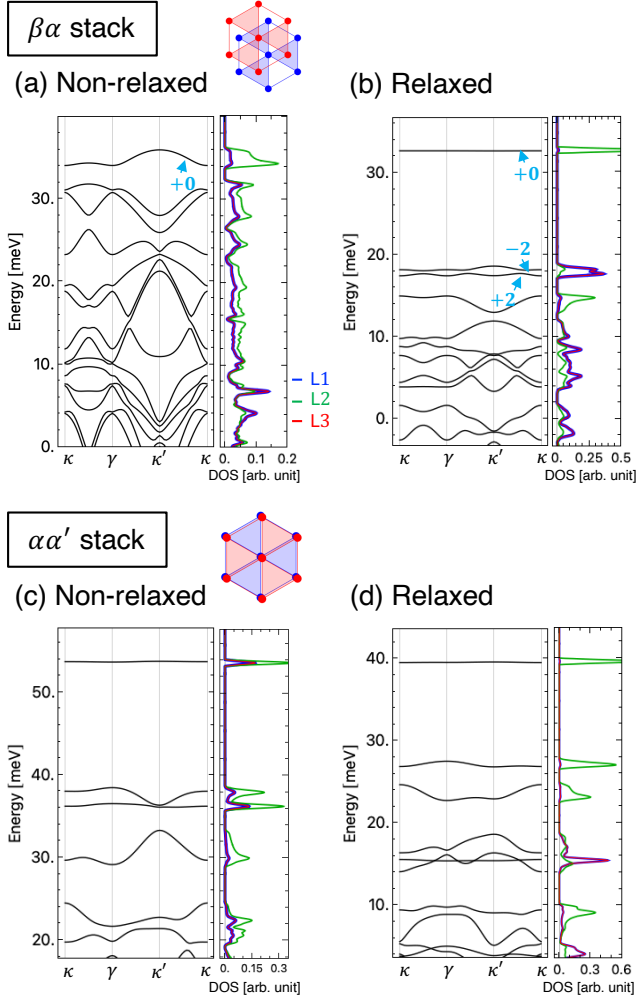


FIG. 13. (Top) Energy band structure near the valence edge of (a) non-relaxed and (b) relaxed $\beta\alpha$ -stacked twisted trilayer WSe₂ with $(\theta^{12}, \theta^{23}) = (+1.0^\circ, +1.0^\circ)$. (Bottom) The similar plot for the $\alpha\alpha'$ stacking.

effective magnetic field. Here we assume $\Delta h_B = 2\Delta h_A$, reflecting the fact that the displacement vector from lattice relaxation on layer 2 is approximately twice as large as that on layer 3.

Figure 14(b) shows the band structure in different values of $\delta_{AB} \equiv E_A - E_B$, with $(\Delta h_A, \Delta h_B, t_{pp}^{AA}, t_{pp}^{BB}, t_{pp}^{AB}) = (5, 10, -0.8, -0.4, -1)$. At $\delta_{AB} = 6$, we observe that the Dirac cones and flat bands are nearly degenerate at a single energy, showing a qualitative agreement with the band structure at $\Delta_E = 20\text{meV}$ in Fig. 9(c).

2. s-p honeycomb model

In a similar manner, the energy band structure in Fig.9(d) can be described by an effective s - p orbital model. We consider a honeycomb lattice composed of

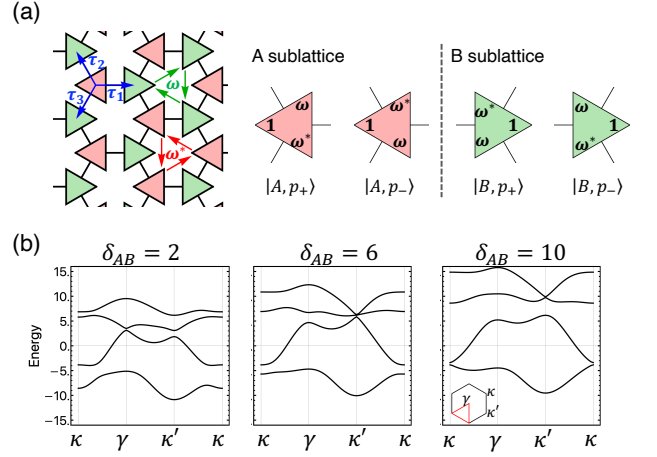


FIG. 14. (a) Schematic illustration of p - p honeycomb model and the orbital $|X, p_\pm\rangle$ ($X = A, B$). The numbers 1, ω, ω^* represent the phase of the wavefunction at triangle corners. (b) Energy band structures of the p - p honeycomb model for different values of $\delta_{AB} = E_A - E_B$, with parameters $(\Delta h_A, \Delta h_B, t_{pp}^{AA}, t_{pp}^{BB}, t_{pp}^{AB}) = (+5, +10, -0.8, -0.4, -1)$. The model qualitatively captures the band structure shown in Fig. 9(c).

an isotropic orbital $|s\rangle$ at the A site, and two orbitals, $|p_+\rangle$ and $|p_-\rangle$, at the B site, as illustrated in Fig.15(a). The Hamiltonian in the basis $(|s\rangle, |p_+\rangle, |p_-\rangle)$ is given by,

$$H_{sp} = \begin{pmatrix} E_s + h_s & u_{p_+,s}^* & u_{p_-,s}^* \\ u_{p_+,s} & E_{p_+} + h_{p_+} & h_{p_-,p_+}^* \\ u_{p_-,s} & h_{p_-,p_+} & E_{p_-} + h_{p_-} \end{pmatrix}, \quad (\text{E6})$$

where E_μ for $(\mu = s, p_+, p_-)$ are the constant on-site energy, and $u_{\mu\nu}$ is the nearest-neighbor hopping terms defined as

$$u_{p_+,s}(\mathbf{k}) = t_{sp} \left[(\omega + \omega^*) e^{-i\mathbf{k}\cdot\boldsymbol{\tau}_1} + (1 + \omega^*) e^{-i\mathbf{k}\cdot\boldsymbol{\tau}_2} + (1 + \omega) e^{-i\mathbf{k}\cdot\boldsymbol{\tau}_3} \right],$$

$$u_{p_-,s}(\mathbf{k}) = (\omega \leftrightarrow \omega^* \text{ in } u_{p_+,s}). \quad (\text{E7})$$

The h_μ and $h_{\mu\nu}$ are the next nearest-neighbor hopping at the same sublattice, which are given by

$$h_s(\mathbf{k}) = t_{ss} \sum_{j=1}^6 e^{-i\mathbf{k}\cdot\mathbf{a}_j},$$

$$h_{p_+}(\mathbf{k}) = t_{pp} \left[\sum_{j=1,3,5} \omega^* e^{-i\mathbf{k}\cdot\mathbf{a}_j} + \sum_{j=2,4,6} \omega e^{-i\mathbf{k}\cdot\mathbf{a}_j} \right],$$

$$h_{p_-}(\mathbf{k}) = (\omega \leftrightarrow \omega^* \text{ in } h_{p_+}), \quad (\text{E8})$$

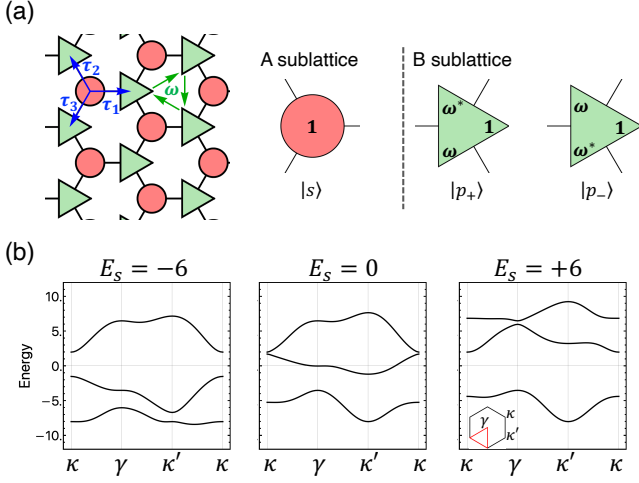


FIG. 15. (a) s - p honeycomb model. (b) Energy band structures of the p - p honeycomb model for different values of E_s , with parameters $(E_{p_+}, E_{p_-}, t_{ss}, t_{pp}, t_{sp}) = (5, -5, 0, -0.5, -1)$, to be compared with Fig. 9(d).

and

$$h_{p_-, p_+}(\mathbf{k}) = t_{pp} \left[\left(e^{-i\mathbf{k}\cdot\mathbf{a}_1} + e^{-i\mathbf{k}\cdot\mathbf{a}_4} \right) + \omega^* \left(e^{-i\mathbf{k}\cdot\mathbf{a}_2} + e^{-i\mathbf{k}\cdot\mathbf{a}_5} \right) + \omega \left(e^{-i\mathbf{k}\cdot\mathbf{a}_3} + e^{-i\mathbf{k}\cdot\mathbf{a}_6} \right) \right]. \quad (\text{E9})$$

In the above formula, we adopt similar definitions of \mathbf{a}_j and $\boldsymbol{\tau}_j$ to Sec. E 1.

The band structure of this model shows a quantitative agreement with the result of Fig 9(d), where the dependence of E_s corresponds to the electric field on-site energy Δ_E . Here, we adopted the parameters of the effective model as $(E_{p_+}, E_{p_-}, t_{ss}, t_{pp}, t_{sp}) = (+5, -5, +0, -0.5, -1)$.

3. d triangular model

The Dirac and flat bands shown in Fig. 10 can be understood by a triangular lattice model with the 3 orbits $|j\rangle = 0, \pm 1$ with with C_{3z} eigenvalue of ω^j . The Hamiltonian in the basis $(|0\rangle, |+\rangle, |-\rangle)$ is given

$$H_d = \begin{pmatrix} E_0 + h_0 & h_{+,0}^* & h_{-,0}^* \\ h_{+,0} & E_+ + h_+ & h_{-,+}^* \\ h_{-,0} & h_{-,+} & E_- + h_- \end{pmatrix}. \quad (\text{E10})$$

E_μ for $(\mu = 0, +, -)$ are the constant on-site energy. Here the intra-orbit hopping terms are defined by

$$h_0(\mathbf{k}) = t \sum_{j=1}^6 e^{-i\mathbf{k}\cdot\mathbf{a}_j},$$

$$h_+(\mathbf{k}) = \tilde{t} \left[\sum_{j=1,3,5} \omega e^{-i\mathbf{k}\cdot\mathbf{a}_j} + \sum_{j=2,4,6} \omega^* e^{-i\mathbf{k}\cdot\mathbf{a}_m} \right],$$

$$h_-(\mathbf{k}) = (\omega \leftrightarrow \omega^* \text{ in } h_+). \quad (\text{E11})$$

The inter-orbits hopping terms are given by

$$h_{+,0}(\mathbf{k}) = t \left[\omega^* \left(e^{-i\mathbf{k}\cdot\mathbf{a}_6} + e^{-i\mathbf{k}\cdot\mathbf{a}_1} \right) + \left(e^{-i\mathbf{k}\cdot\mathbf{a}_2} + e^{-i\mathbf{k}\cdot\mathbf{a}_3} \right) + \omega \left(e^{-i\mathbf{k}\cdot\mathbf{a}_4} + e^{-i\mathbf{k}\cdot\mathbf{a}_5} \right) \right]$$

$$h_{-,0}(\mathbf{k}) = (\omega \leftrightarrow \omega^* \text{ in } h_{+,0}), \quad (\text{E12})$$

and

$$h_{-,+}(\mathbf{k}) = \tilde{t} \left[\left(e^{-i\mathbf{k}\cdot\mathbf{a}_1} + e^{-i\mathbf{k}\cdot\mathbf{a}_4} \right) + \omega^* \left(e^{-i\mathbf{k}\cdot\mathbf{a}_2} + e^{-i\mathbf{k}\cdot\mathbf{a}_5} \right) + \omega \left(e^{-i\mathbf{k}\cdot\mathbf{a}_3} + e^{-i\mathbf{k}\cdot\mathbf{a}_6} \right) \right]. \quad (\text{E13})$$

Figure 16(b) shows the band structure of the model with parameters $(E_0, E_+, E_-, t, \tilde{t}) = (-4, 3, -3, -1, -0.5)$, chosen to qualitatively reproduce the band structure in Fig. 10. We observe a nearly degenerate Dirac band and flat band structure similar to Fig. 10. Notably, this flat band is a remnant of a perfectly flat band realized in a special case with $(E_0, E_+, E_-, t, \tilde{t}) = (-3, 3, -3, -1, -1)$, as shown in Fig.16(c).

Appendix F: Effect of perpendicular electric field in $\alpha\beta$ and $\beta\alpha$ stacking

Figure 17 shows the electric field dependence of the band structure for $\alpha\beta$ - and $\beta\alpha$ -stacked twisted trilayer WSe₂ with $(\theta^{12}, \theta^{23}) = (+1.0^\circ, +1.0^\circ)$, corresponding to Fig. 9 for the $\alpha\alpha'$ stacking. In both cases, we observe the layer polarization switching by the electric field, similar to those seen in the $\alpha\alpha'$ trilayer. The $\alpha\beta$ stacking hosts the kagome lattice state polarized on layer 2, and it can be hybridized with the triangular lattice state of layer 1 and 3 under the perpendicular electric field. At $\Delta_E \approx 12$ meV, in particular, the kagome lattice and s -orbital triangular lattice on layer 3 are hybridized as shown in Fig. 17(b). For $\beta\alpha$ stacking, we find a hybrid band formed by the s state of layer 2 and the p state of layer 3, similar to the band observed in $\alpha\alpha'$ stacking [Fig. 9(d)].

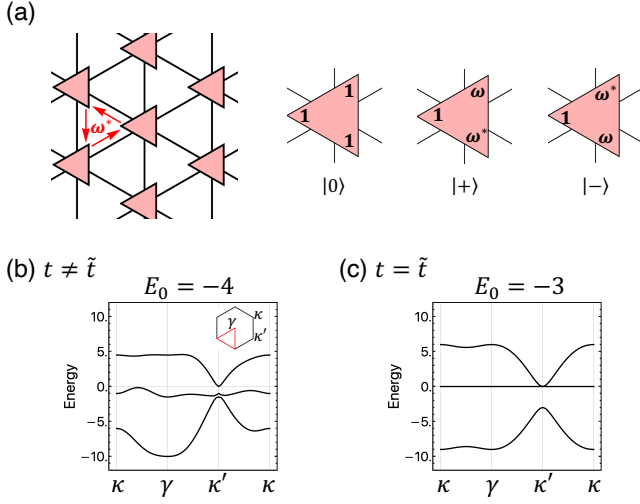


FIG. 16. (a) d -orbital triangular model. (b) Band structure at $(E_0, E_+, E_-, t, \tilde{t}) = (-4, +3, -3, -1, -0.5)$, to be compared with Fig. 10. (c) Band structure with $(E_0, E_+, E_-, t, \tilde{t}) = (-3, +3, -3, -1, -1)$, where a perfect flat band appears.

- ¹ R. Bistritzer and A. MacDonald, Proc. Natl. Acad. Sci. **108**, 12233 (2011).
- ² R. Bistritzer and A. H. MacDonald, Phys. Rev. B **84**, 035440 (2011).
- ³ J. M. B. Lopes dos Santos, N. M. R. Peres, and A. H. Castro Neto, Phys. Rev. B **86**, 155449 (2012).
- ⁴ Y. Cao, V. Fatemi, A. Demir, S. Fang, S. L. Tomarken, J. Y. Luo, J. D. Sanchez-Yamagishi, K. Watanabe, T. Taniguchi, E. Kaxiras, R. C. Ashoori, and P. Jarillo-Herrero, Nature **556**, 80 (2018).
- ⁵ Y. Cao, V. Fatemi, S. Fang, K. Watanabe, T. Taniguchi, E. Kaxiras, and P. Jarillo-Herrero, Nature **556**, 43 (2018).
- ⁶ M. Yankowitz, S. Chen, H. Polshyn, Y. Zhang, K. Watanabe, T. Taniguchi, D. Graf, A. F. Young, and C. R. Dean, Science **363**, 1059 (2019), <https://www.science.org/doi/pdf/10.1126/science.aav1910>.
- ⁷ A. Kerelsky, L. J. McGilly, D. M. Kennes, L. Xian, M. Yankowitz, S. Chen, K. Watanabe, T. Taniguchi, J. Hone, C. Dean, A. Rubio, and A. N. Pasupathy, Nature **572**, 95 (2019).
- ⁸ Y. Xie, B. Lian, B. Jäck, X. Liu, C.-L. Chiu, K. Watanabe, T. Taniguchi, B. A. Bernevig, and A. Yazdani, Nature **572**, 101 (2019).
- ⁹ Y. Jiang, X. Lai, K. Watanabe, T. Taniguchi, K. Haule, J. Mao, and E. Y. Andrei, Nature **573**, 91 (2019).
- ¹⁰ H. Polshyn, M. Yankowitz, S. Chen, Y. Zhang, K. Watanabe, T. Taniguchi, C. R. Dean, and A. F. Young, Nature Physics **15**, 1011 (2019).
- ¹¹ Y. Choi, J. Kemmer, Y. Peng, A. Thomson, H. Arora, R. Polski, Y. Zhang, H. Ren, J. Alicea, G. Refael, F. von Oppen, K. Watanabe, T. Taniguchi, and S. Nadj-Perge, Nature Physics **15**, 1174 (2019).
- ¹² A. L. Sharpe, E. J. Fox, A. W. Barnard, J. Finney, K. Watanabe, T. Taniguchi, M. A. Kastner, and D. Goldhaber-Gordon, Science **365**, 605 (2019), <https://www.science.org/doi/pdf/10.1126/science.aaw3780>.
- ¹³ X. Lu, P. Stepanov, W. Yang, M. Xie, M. A. Aamir, I. Das, C. Urgell, K. Watanabe, T. Taniguchi, G. Zhang, A. Bachtold, A. H. MacDonald, and D. K. Efetov, Nature **574**, 653 (2019).
- ¹⁴ Y. Cao, D. Chowdhury, D. Rodan-Legrain, O. Rubies-Bigorda, K. Watanabe, T. Taniguchi, T. Senthil, and P. Jarillo-Herrero, Phys. Rev. Lett. **124**, 076801 (2020).
- ¹⁵ M. Serlin, C. L. Tschirhart, H. Polshyn, Y. Zhang, J. Zhu, K. Watanabe, T. Taniguchi, L. Balents, and A. F. Young, Science **367**, 900 (2020), <https://www.science.org/doi/pdf/10.1126/science.aay5533>.
- ¹⁶ G. Chen, A. L. Sharpe, E. J. Fox, Y.-H. Zhang, S. Wang, L. Jiang, B. Lyu, H. Li, K. Watanabe, T. Taniguchi, *et al.*, Nature **579**, 56 (2020).
- ¹⁷ Y. Saito, J. Ge, K. Watanabe, T. Taniguchi, and A. F. Young, Nature Physics **16**, 926 (2020).
- ¹⁸ U. Zondiner, A. Rozen, D. Rodan-Legrain, Y. Cao, R. Queiroz, T. Taniguchi, K. Watanabe, Y. Oreg, F. von Oppen, A. Stern, *et al.*, Nature **582**, 203 (2020).
- ¹⁹ D. Wong, K. P. Nuckolls, M. Oh, B. Lian, Y. Xie, S. Jeon, K. Watanabe, T. Taniguchi, B. A. Bernevig, and A. Yazdani, Nature **582**, 198 (2020).
- ²⁰ P. Stepanov, I. Das, X. Lu, A. Fahimniya, K. Watanabe, T. Taniguchi, F. H. Koppens, J. Lischner, L. Levitov, and D. K. Efetov, Nature **583**, 375 (2020).
- ²¹ H. S. Arora, R. Polski, Y. Zhang, A. Thomson, Y. Choi, H. Kim, Z. Lin, I. Z. Wilson, X. Xu, J.-H. Chu, *et al.*, Nature **583**, 379 (2020).
- ²² P. Stepanov, M. Xie, T. Taniguchi, K. Watanabe, X. Lu, A. H. MacDonald, B. A. Bernevig, and D. K. Efetov,

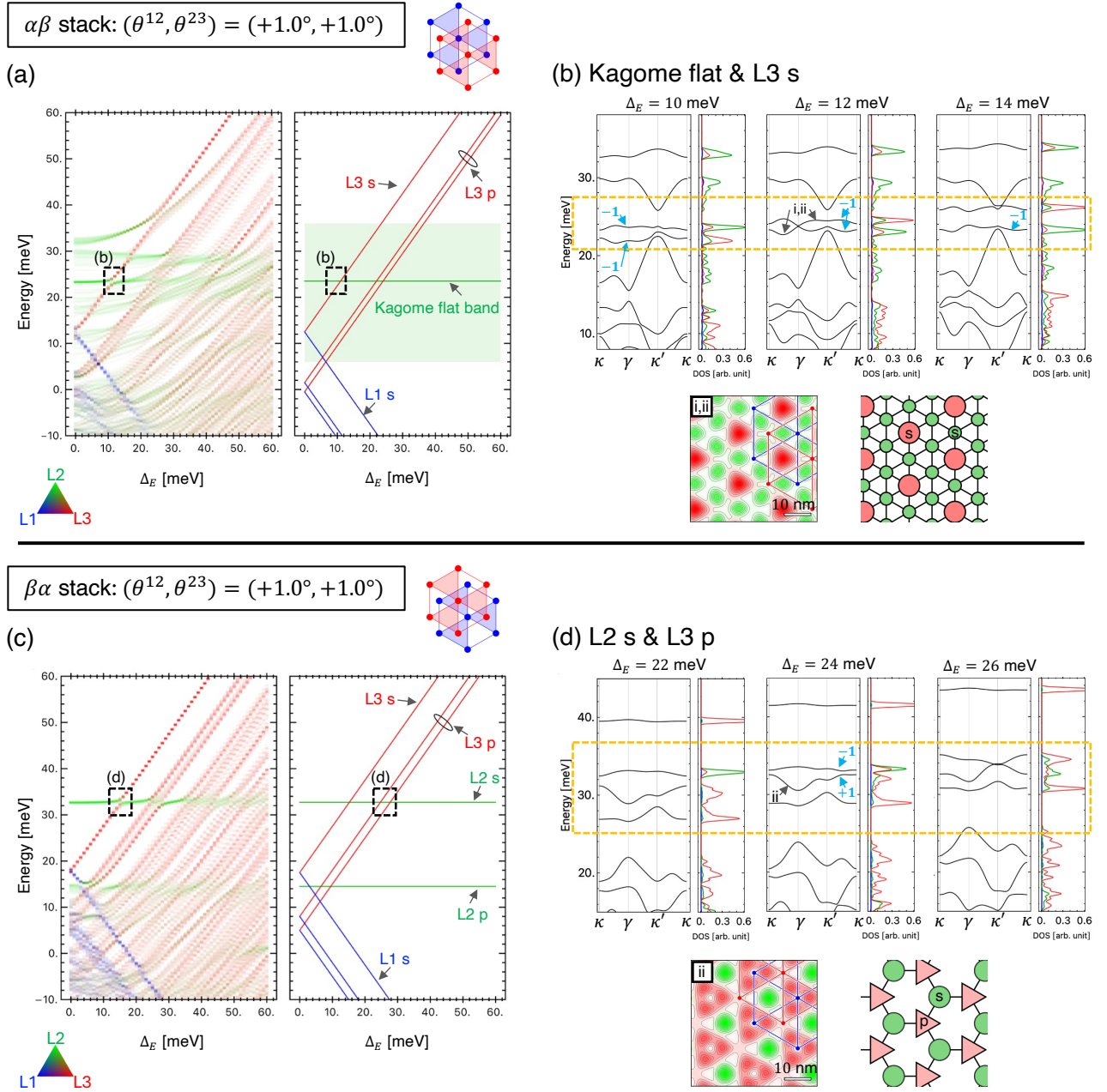


FIG. 17. Perpendicular electric field dependence of the energy band structure for $\alpha\beta$ and $\beta\alpha$ stacking twisted trilayer WSe₂ with helical twist with $(\theta^{12}, \theta^{23}) = (1.0, 1.0)$, corresponding to Fig. 9 for $\alpha\alpha'$ stacking.

- Phys. Rev. Lett. **127**, 197701 (2021).
- ²³ F. Wu, T. Lovorn, E. Tutuc, and A. H. MacDonald, Phys. Rev. Lett. **121**, 026402 (2018).
- ²⁴ H. Pan, F. Wu, and S. Das Sarma, Phys. Rev. Res. **2**, 033087 (2020).
- ²⁵ H. Pan, F. Wu, and S. Das Sarma, Phys. Rev. B **102**, 201104 (2020).
- ²⁶ H. Pan and S. Das Sarma, Phys. Rev. Lett. **127**, 096802 (2021).
- ²⁷ J. Zang, J. Wang, J. Cano, and A. J. Millis, Phys. Rev. B **104**, 075150 (2021).
- ²⁸ M.-H. Zare and H. Mosadeq, Phys. Rev. B **104**, 115154 (2021).
- ²⁹ J. Zang, J. Wang, J. Cano, A. Georges, and A. J. Millis, Phys. Rev. X **12**, 021064 (2022).
- ³⁰ J. Wang, J. Zang, J. Cano, and A. J. Millis, Phys. Rev. Res. **5**, L012005 (2023).
- ³¹ X. Liu, Y. He, C. Wang, X.-W. Zhang, T. Cao, and D. Xiao, Phys. Rev. Lett. **132**, 146401 (2024).
- ³² D. Guerci, K. P. Lucht, V. Crépel, J. Cano, J. H. Pixley, and A. Millis, Phys. Rev. B **110**, 165128 (2024).

- ³³ J. Venderley and E.-A. Kim, Phys. Rev. B **100**, 060506 (2019).
- ³⁴ M. Bélanger, J. Fournier, and D. Sénéchal, Phys. Rev. B **106**, 235135 (2022).
- ³⁵ L. Klebl, A. Fischer, L. Classen, M. M. Scherer, and D. M. Kennes, Phys. Rev. Res. **5**, L012034 (2023).
- ³⁶ Y.-M. Wu, Z. Wu, and H. Yao, Phys. Rev. Lett. **130**, 126001 (2023).
- ³⁷ V. Crépel, D. Guerci, J. Cano, J. H. Pixley, and A. Millis, Phys. Rev. Lett. **131**, 056001 (2023).
- ³⁸ M. Zegrodnik and A. Biborski, Phys. Rev. B **108**, 064506 (2023).
- ³⁹ B. Zhou and Y.-H. Zhang, Phys. Rev. B **108**, 155111 (2023).
- ⁴⁰ C. Schrade and L. Fu, Phys. Rev. B **110**, 035143 (2024).
- ⁴¹ S. Kim, J. F. Mendez-Valderrama, X. Wang, and D. Chowdhury, Nature Communications **16**, 1701 (2025).
- ⁴² Y.-T. Hsu, F. Wu, and S. Das Sarma, Phys. Rev. B **104**, 195134 (2021).
- ⁴³ L. Wang, E.-M. Shih, A. Ghiotto, L. Xian, D. A. Rhodes, C. Tan, M. Claassen, D. M. Kennes, Y. Bai, B. Kim, *et al.*, Nature materials **19**, 861 (2020).
- ⁴⁴ L. An, X. Cai, D. Pei, M. Huang, Z. Wu, Z. Zhou, J. Lin, Z. Ying, Z. Ye, X. Feng, R. Gao, C. Cacho, M. Watson, Y. Chen, and N. Wang, Nanoscale Horiz. **5**, 1309 (2020).
- ⁴⁵ Y. Xia, Z. Han, K. Watanabe, T. Taniguchi, J. Shan, and K. F. Mak, Nature **637**, 833 (2025).
- ⁴⁶ Y. Guo, J. Pack, J. Swann, L. Holtzman, M. Cothrine, K. Watanabe, T. Taniguchi, D. G. Mandrus, K. Barmak, J. Hone, *et al.*, Nature **637**, 839 (2025).
- ⁴⁷ F. Wu, T. Lovorn, and A. H. MacDonald, Phys. Rev. Lett. **118**, 147401 (2017).
- ⁴⁸ H. Yu, G.-B. Liu, J. Tang, X. Xu, and W. Yao, Science advances **3**, e1701696 (2017).
- ⁴⁹ F. Wu, T. Lovorn, and A. H. MacDonald, Phys. Rev. B **97**, 035306 (2018).
- ⁵⁰ K. L. Seyler, P. Rivera, H. Yu, N. P. Wilson, E. L. Ray, D. G. Mandrus, J. Yan, W. Yao, and X. Xu, Nature **567**, 66 (2019).
- ⁵¹ C. Jin, E. C. Regan, A. Yan, M. Iqbal Bakti Utama, D. Wang, S. Zhao, Y. Qin, S. Yang, Z. Zheng, S. Shi, *et al.*, Nature **567**, 76 (2019).
- ⁵² K. Tran, G. Moody, F. Wu, X. Lu, J. Choi, K. Kim, A. Rai, D. A. Sanchez, J. Quan, A. Singh, *et al.*, Nature **567**, 71 (2019).
- ⁵³ D. A. Ruiz-Tijerina and V. I. Fal'ko, Phys. Rev. B **99**, 125424 (2019).
- ⁵⁴ D. Huang, J. Choi, C.-K. Shih, and X. Li, Nature nanotechnology **17**, 227 (2022).
- ⁵⁵ I. Soltero, M. A. Kaliteevski, J. G. McHugh, V. Enaldiev, and V. I. Fal'ko, Nano Letters **24**, 1996 (2024), pMID: 38295286, <https://doi.org/10.1021/acs.nanolett.3c04427>.
- ⁵⁶ F. Wu, T. Lovorn, E. Tutuc, I. Martin, and A. H. MacDonald, Phys. Rev. Lett. **122**, 086402 (2019).
- ⁵⁷ H. Yu, M. Chen, and W. Yao, National Science Review **7**, 12 (2019), <https://academic.oup.com/nsr/article-pdf/7/1/12/40810220/nsr.7.1.12.pdf>.
- ⁵⁸ T. Li, S. Jiang, B. Shen, Y. Zhang, L. Li, Z. Tao, T. Devakul, K. Watanabe, T. Taniguchi, L. Fu, *et al.*, Nature **600**, 641 (2021).
- ⁵⁹ T. Devakul, V. Crépel, Y. Zhang, and L. Fu, Nature communications **12**, 6730 (2021).
- ⁶⁰ Y.-M. Xie, C.-P. Zhang, J.-X. Hu, K. F. Mak, and K. T. Law, Phys. Rev. Lett. **128**, 026402 (2022).
- ⁶¹ J. Cai, E. Anderson, C. Wang, X. Zhang, X. Liu, W. Holtzmann, Y. Zhang, F. Fan, T. Taniguchi, K. Watanabe, *et al.*, Nature **622**, 63 (2023).
- ⁶² Y. Zeng, Z. Xia, K. Kang, J. Zhu, P. Knüppel, C. Vaswani, K. Watanabe, T. Taniguchi, K. F. Mak, and J. Shan, Nature **622**, 69 (2023).
- ⁶³ H. Park, J. Cai, E. Anderson, Y. Zhang, J. Zhu, X. Liu, C. Wang, W. Holtzmann, C. Hu, Z. Liu, *et al.*, Nature **622**, 74 (2023).
- ⁶⁴ F. Xu, Z. Sun, T. Jia, C. Liu, C. Xu, C. Li, Y. Gu, K. Watanabe, T. Taniguchi, B. Tong, J. Jia, Z. Shi, S. Jiang, Y. Zhang, X. Liu, and T. Li, Phys. Rev. X **13**, 031037 (2023).
- ⁶⁵ N. Morales-Durán, N. Wei, J. Shi, and A. H. MacDonald, Phys. Rev. Lett. **132**, 096602 (2024).
- ⁶⁶ B. A. Foutty, C. R. Kometter, T. Devakul, A. P. Reddy, K. Watanabe, T. Taniguchi, L. Fu, and B. E. Feldman, Science **384**, 343 (2024), <https://www.science.org/doi/pdf/10.1126/science.adi4728>.
- ⁶⁷ Y. Jia, J. Yu, J. Liu, J. Herzog-Arbeitman, Z. Qi, H. Pi, N. Regnault, H. Weng, B. A. Bernevig, and Q. Wu, Phys. Rev. B **109**, 205121 (2024).
- ⁶⁸ X.-W. Zhang, C. Wang, X. Liu, Y. Fan, T. Cao, and D. Xiao, Nature Communications **15**, 4223 (2024).
- ⁶⁹ J. Shi, N. Morales-Durán, E. Khalaf, and A. H. MacDonald, Phys. Rev. B **110**, 035130 (2024).
- ⁷⁰ H. Li, U. Kumar, K. Sun, and S.-Z. Lin, Phys. Rev. Res. **3**, L032070 (2021).
- ⁷¹ V. Crépel and L. Fu, Phys. Rev. B **107**, L201109 (2023).
- ⁷² A. P. Reddy, F. Alsallom, Y. Zhang, T. Devakul, and L. Fu, Phys. Rev. B **108**, 085117 (2023).
- ⁷³ N. Morales-Durán, J. Wang, G. R. Schleder, M. Angeli, Z. Zhu, E. Kaxiras, C. Repellin, and J. Cano, Phys. Rev. Res. **5**, L032022 (2023).
- ⁷⁴ J. Dong, J. Wang, P. J. Ledwith, A. Vishwanath, and D. E. Parker, Phys. Rev. Lett. **131**, 136502 (2023).
- ⁷⁵ C. Wang, X.-W. Zhang, X. Liu, Y. He, X. Xu, Y. Ran, T. Cao, and D. Xiao, Phys. Rev. Lett. **132**, 036501 (2024).
- ⁷⁶ J. Yu, J. Herzog-Arbeitman, M. Wang, O. Vafek, B. A. Bernevig, and N. Regnault, Phys. Rev. B **109**, 045147 (2024).
- ⁷⁷ C. Xu, J. Li, Y. Xu, Z. Bi, and Y. Zhang, Proceedings of the National Academy of Sciences **121**, e2316749121 (2024), <https://www.pnas.org/doi/pdf/10.1073/pnas.2316749121>.
- ⁷⁸ X.-Y. Song, Y.-H. Zhang, and T. Senthil, Phys. Rev. B **109**, 085143 (2024).
- ⁷⁹ A. Abouelkomsan, A. P. Reddy, L. Fu, and E. J. Bergholtz, Phys. Rev. B **109**, L121107 (2024).
- ⁸⁰ F. Chen, W.-W. Luo, W. Zhu, and D. Sheng, Nature Communications **16**, 2115 (2025).
- ⁸¹ B. Li and F. Wu, Phys. Rev. B **111**, 125122 (2025).
- ⁸² N. Paul, A. Abouelkomsan, A. Reddy, and L. Fu, arXiv preprint arXiv:2502.17569 (2025).
- ⁸³ K. Kang, Y. Qiu, B. Shen, K. Lee, Z. Xia, Y. Zeng, K. Watanabe, T. Taniguchi, J. Shan, and K. F. Mak, arXiv preprint arXiv:2501.02525 (2025).
- ⁸⁴ B. M. Kousa, N. Morales-Durán, T. M. Wolf, E. Khalaf, and A. H. MacDonald, arXiv preprint arXiv:2502.17574 (2025).
- ⁸⁵ J. Shi, J. Cano, and N. Morales-Durán, arXiv preprint arXiv:2503.15900 (2025).

- ⁸⁶ T. Zaklama, D. Luo, and L. Fu, arXiv preprint arXiv:2411.03496 (2024).
- ⁸⁷ A. P. Reddy, D. Sheng, A. Abouelkomsan, E. J. Bergholtz, and L. Fu, arXiv preprint arXiv:2411.19898 (2024).
- ⁸⁸ Y. Tang, L. Li, T. Li, Y. Xu, S. Liu, K. Barmak, K. Watanabe, T. Taniguchi, A. H. MacDonald, J. Shan, *et al.*, *Nature* **579**, 353 (2020).
- ⁸⁹ E. C. Regan, D. Wang, C. Jin, M. I. Bakti Utama, B. Gao, X. Wei, S. Zhao, W. Zhao, Z. Zhang, K. Yumigeta, *et al.*, *Nature* **579**, 359 (2020).
- ⁹⁰ Z. Zhang, Y. Wang, K. Watanabe, T. Taniguchi, K. Ueno, E. Tutuc, and B. J. LeRoy, *Nature Physics* **16**, 1093 (2020).
- ⁹¹ V. V. Enaldiev, V. Zólyomi, C. Yelgel, S. J. Magorrian, and V. I. Fal'ko, *Phys. Rev. Lett.* **124**, 206101 (2020).
- ⁹² Y. Xu, S. Liu, D. A. Rhodes, K. Watanabe, T. Taniguchi, J. Hone, V. Elser, K. F. Mak, and J. Shan, *Nature* **587**, 214 (2020).
- ⁹³ M. Angeli and A. H. MacDonald, *Proceedings of the National Academy of Sciences* **118**, e2021826118 (2021), <https://www.pnas.org/doi/pdf/10.1073/pnas.2021826118>.
- ⁹⁴ H. Li, S. Li, E. C. Regan, D. Wang, W. Zhao, S. Kahn, K. Yumigeta, M. Blei, T. Taniguchi, K. Watanabe, *et al.*, *Nature* **597**, 650 (2021).
- ⁹⁵ X. Wang, K. Yasuda, Y. Zhang, S. Liu, K. Watanabe, T. Taniguchi, J. Hone, L. Fu, and P. Jarillo-Herrero, *Nature nanotechnology* **17**, 367 (2022).
- ⁹⁶ V. V. Enaldiev, F. Ferreira, and V. I. Fal'ko, *Nano Letters* **22**, 1534 (2022).
- ⁹⁷ E. Anderson, F.-R. Fan, J. Cai, W. Holtzmann, T. Taniguchi, K. Watanabe, D. Xiao, W. Yao, and X. Xu, *Science* **381**, 325 (2023), <https://www.science.org/doi/pdf/10.1126/science.adg4268>.
- ⁹⁸ K. c. v. Kolář, K. Yang, F. von Oppen, and C. Mora, *Phys. Rev. B* **110**, 115114 (2024).
- ⁹⁹ Z. Song, Y. Wang, H. Zheng, P. Narang, and L.-W. Wang, *Journal of the American Chemical Society* **144**, 14657 (2022).
- ¹⁰⁰ V. Enaldiev, F. Ferreira, J. McHugh, and V. I. Fal'ko, *npj 2D Materials and Applications* **6**, 74 (2022).
- ¹⁰¹ W. Pasek, M. Kupczynski, and P. Potasz, *Phys. Rev. B* **108**, 165152 (2023).
- ¹⁰² I. Soltero, M. A. Kaliteevski, J. G. McHugh, V. Enaldiev, and V. I. Fal'ko, *Nano Letters* **24**, 1996 (2024).
- ¹⁰³ L. Cavicchi, K. J. Reijnders, M. I. Katsnelson, and M. Polini, arXiv preprint arXiv:2410.18025 (2024).
- ¹⁰⁴ C. Mora, N. Regnault, and B. A. Bernevig, *Phys. Rev. Lett.* **123**, 026402 (2019).
- ¹⁰⁵ X. Li, F. Wu, and A. H. MacDonald, "Electronic structure of single-twist trilayer graphene," (2019), arXiv:1907.12338 [cond-mat.mtrl-sci].
- ¹⁰⁶ S. Carr, C. Li, Z. Zhu, E. Kaxiras, S. Sachdev, and A. Kruchkov, *Nano Letters* **20**, 3030 (2020), pMID: 32208724, <https://doi.org/10.1021/acs.nanolett.9b04979>.
- ¹⁰⁷ G. A. Tritsarlis, S. Carr, Z. Zhu, Y. Xie, S. B. Torrisi, J. Tang, M. Mattheakis, D. T. Larson, and E. Kaxiras, *2D Materials* **7**, 035028 (2020).
- ¹⁰⁸ A. Lopez-Bezanilla and J. L. Lado, *Phys. Rev. Res.* **2**, 033357 (2020).
- ¹⁰⁹ A. Ramires and J. L. Lado, *Phys. Rev. Lett.* **127**, 026401 (2021).
- ¹¹⁰ C. Lei, L. Linhart, W. Qin, F. Libisch, and A. H. MacDonald, *Phys. Rev. B* **104**, 035139 (2021).
- ¹¹¹ V. o. T. Phong, P. A. Pantaleón, T. Cea, and F. Guinea, *Phys. Rev. B* **104**, L121116 (2021).
- ¹¹² D. Călugăru, F. Xie, Z.-D. Song, B. Lian, N. Regnault, and B. A. Bernevig, *Phys. Rev. B* **103**, 195411 (2021).
- ¹¹³ F. Xie, N. Regnault, D. Călugăru, B. A. Bernevig, and B. Lian, *Phys. Rev. B* **104**, 115167 (2021).
- ¹¹⁴ D. Guerci, P. Simon, and C. Mora, *Phys. Rev. Res.* **4**, L012013 (2022).
- ¹¹⁵ T. Devakul, P. J. Ledwith, L.-Q. Xia, A. Uri, S. C. de la Barrera, P. Jarillo-Herrero, and L. Fu, *Science Advances* **9**, eadi6063 (2023), <https://www.science.org/doi/pdf/10.1126/sciadv.adi6063>.
- ¹¹⁶ M. Christos, S. Sachdev, and M. S. Scheurer, *Phys. Rev. X* **12**, 021018 (2022).
- ¹¹⁷ Y. Zhang, R. Polski, C. Lewandowski, A. Thomson, Y. Peng, Y. Choi, H. Kim, K. Watanabe, T. Taniguchi, J. Alicea, F. von Oppen, G. Refael, and S. Nadj-Perge, *Science* **377**, 1538 (2022), <https://www.science.org/doi/pdf/10.1126/science.abn8585>.
- ¹¹⁸ Z. Hao, A. M. Zimmerman, P. Ledwith, E. Khalaf, D. H. Najafabadi, K. Watanabe, T. Taniguchi, A. Vishwanath, and P. Kim, *Science* **371**, 1133 (2021), <https://www.science.org/doi/pdf/10.1126/science.abg0399>.
- ¹¹⁹ J. M. Park, Y. Cao, K. Watanabe, T. Taniguchi, and P. Jarillo-Herrero, *Nature* **590**, 249 (2021).
- ¹²⁰ Y. Cao, J. M. Park, K. Watanabe, T. Taniguchi, and P. Jarillo-Herrero, *Nature* **595**, 526 (2021).
- ¹²¹ H. Kim, Y. Choi, C. Lewandowski, A. Thomson, Y. Zhang, R. Polski, K. Watanabe, T. Taniguchi, J. Alicea, and S. Nadj-Perge, *Nature* **606**, 494 (2022).
- ¹²² Z. Zhu, P. Cazeaux, M. Luskin, and E. Kaxiras, *Phys. Rev. B* **101**, 224107 (2020).
- ¹²³ Z. Zhu, S. Carr, D. Massatt, M. Luskin, and E. Kaxiras, *Phys. Rev. Lett.* **125**, 116404 (2020).
- ¹²⁴ F. Lin, J. Qiao, J. Huang, J. Liu, D. Fu, A. S. Mayorov, H. Chen, P. Mukherjee, T. Qu, C.-H. Sow, *et al.*, *Nano Letters* **20**, 7572 (2020).
- ¹²⁵ X. Zhang, K.-T. Tsai, Z. Zhu, W. Ren, Y. Luo, S. Carr, M. Luskin, E. Kaxiras, and K. Wang, *Phys. Rev. Lett.* **127**, 166802 (2021).
- ¹²⁶ Q. Gao and E. Khalaf, *Physical Review B* **106**, 075420 (2022).
- ¹²⁷ Z. Ma, S. Li, M. Lu, D.-H. Xu, J.-H. Gao, and X. Xie, *Science China Physics, Mechanics & Astronomy* **66**, 227211 (2022).
- ¹²⁸ M. Liang, M.-M. Xiao, Z. Ma, and J.-H. Gao, *Phys. Rev. B* **105**, 195422 (2022).
- ¹²⁹ A. Uri, S. C. de la Barrera, M. T. Randeria, D. Rodan-Legrain, T. Devakul, P. J. Crowley, N. Paul, K. Watanabe, T. Taniguchi, R. Lifshitz, *et al.*, *Nature* **620**, 762 (2023).
- ¹³⁰ Y. Mao, D. Guerci, and C. Mora, *Phys. Rev. B* **107**, 125423 (2023).
- ¹³¹ F. K. Popov and G. Tarnopolsky, *Phys. Rev. B* **108**, L081124 (2023).
- ¹³² X. Lin, C. Li, K. Su, and J. Ni, *Phys. Rev. B* **106**, 075423 (2022).
- ¹³³ H. Meng, Z. Zhan, and S. Yuan, *Phys. Rev. B* **107**, 035109 (2023).
- ¹³⁴ S. Turkel, J. Swann, Z. Zhu, M. Christos, K. Watanabe, T. Taniguchi, S. Sachdev, M. S. Scheurer, E. Kaxiras, C. R. Dean, and A. N. Pasupathy, *Science* **376**, 193 (2022), <https://www.science.org/doi/pdf/10.1126/science.abk1895>.

- 135 I. M. Craig, M. Van Winkle, C. Groschner, K. Zhang, N. Dowlatsahi, Z. Zhu, T. Taniguchi, K. Watanabe, S. M. Griffin, and D. K. Bediako, *Nature Materials* **23**, 323 (2024).
- 136 Y. Li, M. Xue, H. Fan, C.-F. Gao, Y. Shi, Y. Liu, K. Watanabe, T. Tanguchi, Y. Zhao, F. Wu, *et al.*, *Nano Letters* **22**, 6215 (2022).
- 137 J. Shin, Y. Park, B. L. Chittari, J.-H. Sun, and J. Jung, *Physical Review B* **103**, 075423 (2021).
- 138 N. Nakatsuji, T. Kawakami, and M. Koshino, *Phys. Rev. X* **13**, 041007 (2023).
- 139 D. Park, C. Park, E. Ko, K. Yananose, R. Engelke, X. Zhang, K. Davydov, M. Green, S. H. Park, J. H. Lee, *et al.*, arXiv preprint arXiv:2402.15760 (2024).
- 140 H. AlBuhairan and M. Vogl, *Phys. Rev. B* **108**, 155106 (2023).
- 141 M. Liang, S.-P. Ding, M. Wu, C. Zhao, and J.-H. Gao, *Phys. Rev. B* **111**, 085412 (2025).
- 142 H. He, Z. Gong, Q.-J. Tong, D. Zhai, W. Yao, and X.-T. An, *Phys. Rev. B* **111**, 125410 (2025).
- 143 A. Fedorko, C.-X. Liu, and Z. Bi, “Engineering moiré kagome superlattices in twisted transition metal dichalcogenides,” (2025), arXiv:2503.13422 [cond-mat.mes-hall].
- 144 N. Mounet, M. Gibertini, P. Schwaller, D. Campi, A. Merkys, A. Marrazzo, T. Sohier, I. E. Castelli, A. Cepellotti, G. Pizzi, *et al.*, *Nature nanotechnology* **13**, 246 (2018).
- 145 P. Moon and M. Koshino, *Phys. Rev. B* **87**, 205404 (2013).
- 146 N. N. T. Nam and M. Koshino, *Phys. Rev. B* **96**, 075311 (2017), errata *ibid* **101**, 099901 (2020).
- 147 M. Koshino and N. N. Nam, *Phys. Rev. B* **101**, 195425 (2020).
- 148 H. Suzuura and T. Ando, *Phys. Rev. B* **65**, 235412 (2002).
- 149 P. San-Jose, A. Gutiérrez-Rubio, M. Sturla, and F. Guinea, *Phys. Rev. B* **90**, 115152 (2014).
- 150 K. Yananose, C. Park, and Y.-W. Son, “Metamorphic quantum dot arrays in twisted trilayer hexagonal boron nitride,” (2025), arXiv:2504.14925 [cond-mat.mes-hall].
- 151 S. Fang, S. Carr, M. A. Cazalilla, and E. Kaxiras, *Phys. Rev. B* **98**, 075106 (2018).
- 152 B. Fallahazad, H. C. P. Movva, K. Kim, S. Larentis, T. Taniguchi, K. Watanabe, S. K. Banerjee, and E. Tutuc, *Phys. Rev. Lett.* **116**, 086601 (2016).
- 153 F. A. Rasmussen and K. S. Thygesen, *The Journal of Physical Chemistry C* **119**, 13169 (2015).
- 154 S. J. Magorrian, V. V. Enaldiev, V. Zólyomi, F. Ferreira, V. I. Fal’ko, and D. A. Ruiz-Tijerina, *Phys. Rev. B* **104**, 125440 (2021).
- 155 L. C. Towle, V. Oberbeck, B. E. Brown†, and R. E. Stajdohar, *Science* **154**, 895 (1966), <https://www.science.org/doi/pdf/10.1126/science.154.3751.895>.
- 156 R. Suzuki, M. Sakano, Y. Zhang, R. Akashi, D. Morikawa, A. Harasawa, K. Yaji, K. Kuroda, K. Miyamoto, T. Okuda, *et al.*, *Nature nanotechnology* **9**, 611 (2014).
- 157 T. Jiang, H. Liu, D. Huang, S. Zhang, Y. Li, X. Gong, Y.-R. Shen, W.-T. Liu, and S. Wu, *Nature nanotechnology* **9**, 825 (2014).
- 158 F. D. M. Haldane, *Phys. Rev. Lett.* **61**, 2015 (1988).
- 159 D. Sticlet and F. Piéchon, *Phys. Rev. B* **87**, 115402 (2013).
- 160 Z.-W. Chang, W.-C. Hao, and X. Liu, *Journal of Physics: Condensed Matter* **34**, 485502 (2022).
- 161 G. Chang, S.-Y. Xu, B. J. Wieder, D. S. Sanchez, S.-M. Huang, I. Belopolski, T.-R. Chang, S. Zhang, A. Bansil, H. Lin, and M. Z. Hasan, *Phys. Rev. Lett.* **119**, 206401 (2017).
- 162 P. Tang, Q. Zhou, and S.-C. Zhang, *Phys. Rev. Lett.* **119**, 206402 (2017).
- 163 D. Takane, Z. Wang, S. Souma, K. Nakayama, T. Nakamura, H. Oinuma, Y. Nakata, H. Iwasawa, C. Cacho, T. Kim, K. Horiba, H. Kumigashira, T. Takahashi, Y. Ando, and T. Sato, *Phys. Rev. Lett.* **122**, 076402 (2019).
- 164 Y. Yang, H.-x. Sun, J.-p. Xia, H. Xue, Z. Gao, Y. Ge, D. Jia, S.-q. Yuan, Y. Chong, and B. Zhang, *Nature Physics* **15**, 645 (2019).
- 165 D. S. Sanchez, I. Belopolski, T. A. Cochran, X. Xu, J.-X. Yin, G. Chang, W. Xie, K. Manna, V. Süß, C.-Y. Huang, *et al.*, *Nature* **567**, 500 (2019).
- 166 Z. Rao, H. Li, T. Zhang, S. Tian, C. Li, B. Fu, C. Tang, L. Wang, Z. Li, W. Fan, *et al.*, *Nature* **567**, 496 (2019).
- 167 L. Li and M. Wu, *ACS nano* **11**, 6382 (2017).
- 168 Q. Tong, M. Chen, F. Xiao, H. Yu, and W. Yao, *2D Materials* **8**, 025007 (2020).
- 169 F. Ferreira, V. V. Enaldiev, V. I. Fal’ko, and S. J. Magorrian, *Scientific Reports* **11**, 13422 (2021).
- 170 G. Kresse and J. Furthmüller, *Computational Materials Science* **6**, 15 (1996).
- 171 G. Kresse and J. Furthmüller, *Phys. Rev. B* **54**, 11169 (1996).
- 172 J. P. Perdew, K. Burke, and M. Ernzerhof, *Phys. Rev. Lett.* **77**, 3865 (1996).
- 173 S. Grimme, J. Antony, S. Ehrlich, and H. Krieg, *The Journal of Chemical Physics* **132**, 154104 (2010), https://pubs.aip.org/aip/jcp/article-pdf/doi/10.1063/1.3382344/15684000/154104.1_online.pdf.
- 174 S. Steiner, S. Khmelevskiy, M. Marsmann, and G. Kresse, *Phys. Rev. B* **93**, 224425 (2016).
- 175 C. Wu, D. Bergman, L. Balents, and S. Das Sarma, *Phys. Rev. Lett.* **99**, 070401 (2007).
- 176 C. Wu and S. Das Sarma, *Phys. Rev. B* **77**, 235107 (2008).
- 177 G. Tamaki, T. Kawakami, and M. Koshino, *Phys. Rev. B* **101**, 205311 (2020).